

SCIENCE OF TSUNAMI HAZARDS

Journal of Tsunami Society International

Volume 36

Number 2

2017

NUMERICAL MODELING OF MOON ASTEROID IMPACTS TSUNAMIS ON THE MOON

49

Charles L. Mader - *Mader Consulting Co.- Honolulu, HI 96825 U.S.A*

SIMULATION OF SCOURING AROUND A VERTICAL CYLINDER DUE TO TSUNAMI

59

Kuswandi¹, Radiana Triatmadja^{2*}, Istiarto²

¹PhD Student, Department of Civil and Environment Engineering, Faculty of Engineering, Universitas Gadjah Mada, INDONESIA

²Department of Civil and Environmental Engineering, Faculty of Engineering, Universitas Gadjah Mada, INDONESIA.

^{1,2}Member of Tsunami Research Group, Universitas Gadjah Mada, INDONESIA

BENCHMARK SOLUTIONS FOR TSUNAMI WAVE FRONTS AND RAYS. PART 2: PARABOLIC BOTTOM TOPOGRAPHY

70

Andrey. G. Marchuk

Institute of Computational Mathematics and Mathematical Geophysics, Siberian Division of Russian Academy of Sciences, Novosibirsk, RUSSIA

INVESTIGATION OF b-VALUE VARIATIONS IN THE AFRICAN AND PARTS OF EURASIAN PLATES

¹Awoyemi, M. O., ²Hammed O.S., ¹Shode, O. H., ⁴Olurin, O.T., ²Igboama, W.N.
and ³Fatoba, J.O.

86

¹. Department of Physics, Obafemi Awolowo University, Ile-Ife, NIGERIA.

². Department of Physics, Federal University, Oye Ekiti, NIGERIA.

³. Department of Geophysics, Federal University, Oye Ekiti, NIGERIA.

⁴. Department of Physics, Federal University of Agriculture, Abeokuta, NIGERIA.

TSUNAMI SOCIETY INTERNATIONAL, 1741 Ala Moana Blvd. #70, Honolulu, HI 96815, USA.

SCIENCE OF TSUNAMI HAZARDS is a **CERTIFIED OPEN ACCESS** Journal included in the prestigious international academic journal database **DOAJ**, maintained by the University of Lund in Sweden with the support of the European Union. **SCIENCE OF TSUNAMI HAZARDS** is also preserved, archived and disseminated by the National Library, The Hague, **NETHERLANDS**, the Library of Congress, Washington D.C., USA, the Electronic Library of Los Alamos, National Laboratory, New Mexico, USA, the **EBSCO Publishing** databases and **ELSEVIER Publishing** in Amsterdam. The vast dissemination gives the journal additional global exposure and readership in 90% of the academic institutions worldwide, including nationwide access to databases in more than 70 countries.

OBJECTIVE: Tsunami Society International publishes this interdisciplinary journal to increase and disseminate knowledge about tsunamis and their hazards.

DISCLAIMER: Although the articles in **SCIENCE OF TSUNAMI HAZARDS** have been technically reviewed by peers, Tsunami Society International is not responsible for the veracity of any statement, opinion or consequences.

EDITORIAL STAFF

Dr. George Pararas-Carayannis, Editor
<mailto:drgeorgepc@yahoo.com>

EDITORIAL BOARD

Dr. Charles MADER, Mader Consulting Co., Colorado, New Mexico, Hawaii, USA
Dr. Hermann FRITZ, Georgia Institute of Technology, USA
Prof. George CURTIS, University of Hawaii -Hilo, USA
Dr. Tad S. MURTY, University of Ottawa, CANADA
Dr. Zygmunt KOWALIK, University of Alaska, USA
Dr. Galen GISLER, NORWAY
Prof. Kam Tim CHAU, Hong Kong Polytechnic University, HONG KONG
Dr. Jochen BUNDSCHUH, (ICE) COSTA RICA, Royal Institute of Technology, SWEDEN
Dr. Yurii SHOKIN, Novosibirsk, RUSSIAN FEDERATION
Dr. Radiana Triatmadja - Tsunami Research Group, Universitas Gadjah Mada, Yogyakarta, INDONESIA

TSUNAMI SOCIETY INTERNATIONAL, OFFICERS

Dr. George Pararas-Carayannis, President;
Dr. Tad Murty, Vice President;
Dr. Carolyn Forbes, Secretary/Treasurer.

Submit manuscripts of research papers, notes or letters to the Editor. If a research paper is accepted for publication the author(s) must submit a scan-ready manuscript, a Doc, TeX or a PDF file in the journal format. Issues of the journal are published electronically in PDF format. There is a minimal publication fee for authors who are members of Tsunami Society International for three years and slightly higher for non-members. Tsunami Society International members are notified by e-mail when a new issue is available. Permission to use figures, tables and brief excerpts from this journal in scientific and educational works is granted provided that the source is acknowledged.

Recent and all past journal issues are available at: <http://www.TsunamiSociety.org> CD-ROMs of past volumes may be purchased by contacting Tsunami Society International at postmaster@tsunamisociety.org Issues of the journal from 1982 thru 2005 are also available in PDF format at the U.S. Los Alamos National Laboratory Library <http://epubs.lanl.gov/tsunami/>

ISSN 8755-6839



SCIENCE OF TSUNAMI HAZARDS

Journal of Tsunami Society International

Volume 36

Number 2

2017

NUMERICAL MODELING OF MOON ASTEROID IMPACTS TSUNAMIS ON THE MOON

Charles L. Mader

*Mader Consulting Co.
Honolulu, HI 96825 U.S.A.*

ABSTRACT

Asteroid impacts on the moon were modeled using the full Navier-Stokes AMR Eulerian compressible hydrodynamic code called MAGNS. The size of the cavity and its time history are strongly dependent upon the strength characteristics of the moon rock. The initial impact pressures and temperatures are well above shock melting conditions at the impact surface of the moon.

The formation of a moon crater, its rings and mascon is modeled.

Keywords: *Modeling, Navier-Stokes, Eulerian, moon crater, crater rings.*

Vol 36. No. 2, page 49 (2017)

INTRODUCTION

William Van Dorn has proposed models to explain the observed rings in the craters on the moon as described in (Van Dorn, 1968 and 1969) which he calls "Tsunamis on the Moon." He requested modeling of the impact of a 10-kilometer radius basalt or iron asteroid moving at 10 kilometers/second with the moon assuming possible liquid and solid basalt layers.

1 NUMERICAL MODELING

The compressible Navier-Stokes equations are described in (Mader, 2004, 1998) and examples of many numerical solutions of complicated physical problems are described. The compressible Navier-Stokes equations are solved by a high-resolution Godunov differencing scheme using an adaptive grid technique described in (Gittings, 1992).

The solution technique uses Continuous Adaptive Mesh Refinement (CAMR). The decision to refine the grid is made cell-by-cell continuously throughout the calculation. The computing is concentrated on the regions of the problem, which require high resolution.

Refinement occurs when gradients in physical properties (density, pressure, temperature, material constitution) exceed defined limits, down to a specified minimum cell size for each material. The mesh refinement is described in detail in (Mader, 2004).

Much larger computational volumes, times and differences in scale can be simulated than possible using previous Eulerian techniques such as those described in (Mader, 1998).

The original code was called SAGE. A later version with radiation is called RAGE. A recent version with the techniques for modeling reactive flow described in (Mader, 2004) is called NOBEL.

Some of the remarkable advances in fluid physics using the NOBEL code have been the modeling of Richtmyer-Meshkov and shock induced instabilities described in (Holmes et al., 1999 and Baltrusaitis et al., 1996). It was used for modeling the Lituya Bay impact landslide generated tsunami and water cavity generation described in (Mader 1999 and 2002). NOBEL/SAGE/RAGE were used to model the generation of water cavities by projectiles and explosions and the resulting water waves in (Mader and Gittings, 2003). The codes were used to model asteroid impacts with the ocean and the resulting tsunami waves in (Gisler, et al., 2003, 2004).

The codes can describe one-dimensional slab or spherical geometry, two-dimensional slab or cylindrical geometry, and three-dimensional Cartesian geometry.

Because modern supercomputing is currently done on clusters of machines containing many identical processors, the parallel implementation of the code is very important. For portability and scalability, the codes use the Message Passing Interface (MPI). Load leveling is accomplished through the use of an adaptive cell pointer list; in which newly created daughter cells are placed immediately after the mother cells. Cells are redistributed among processors at every time step, while keeping mothers and daughters together. If there are a total of M cells and N processors, this technique gives nearly (M / N) cells per processor. As neighbor cell variables are needed, the MPI gather/scatter routines copy those neighbor variables into local scratch memory.

The calculations described in this paper were performed on IMAC Apple and PC computers and did not require massive parallel computers.

The codes incorporate multiple material equations of state (analytical or SESAME tabular). Every cell can in principle contain a mixture of all the materials in a problem assuming that they are in pressure and temperature equilibrium.

As described in (Mader, 1998), pressure and temperature equilibrium is appropriate only for materials mixed molecularly. The assumption of temperature equilibrium is inappropriate for mixed cells with interfaces between different materials. The errors increase with increasing density differences. While the mixture equations of state described in (Mader, 1998) would be more realistic, the problem is minimized by using fine numerical resolution at interfaces. The amount of mass in mixed cells is kept small resulting in small errors being introduced by the temperature equilibrium assumption.

Very important for late time cavity history is the capability to initialize gravity properly, which is included in the code. This results in the initial density and initial pressure-changing going from the very low-density atmosphere at 20 kilometers altitude down to the moon surface. Likewise the rock density and pressure changes correctly with increasing depth. The moon gravity constant used was 167 vs 980 for the earth.

Soon after the initial impact and the cavity formation is occurring, the previously shocked and compressed rock is being rarefied and pulverized. The rock is called “fluidized” and modeled as described in the modeling of crater formation of the Arizona meteor crater and the SEDAN nuclear crater described in (Mader, 2009).

A new code called MAGNS was used in this study. It has been used to model oblique shock initiation of insensitive explosives described in (Mader and Gittings, 2004).

SUMMARY OF MODELED CAVITY DIMENSIONS

For a 20 kilometer diameter Projectile impacting Moon Crust at 10 kilometer/sec

Problem	Max Depth	Max Diameter	Collapse	
Basalt Projectile, 5.5 kb Basalt Yield	40 km	60 km	No	
Iron Projectile, 5.5 KB Basalt Yield	80 km	90 km	No	
Basalt Projectile, Fluid Basalt	- 1000 s	75 km	120 km	Yes
	- 2000 s	70 km	160 km	
	- 3000 s	30 km	180 km	Axis Jet
Basalt projectile, impacts water	- 1000 s	120 km	120 km	Yes
	- 2000 s	100 km	160 km	
	- 3000 s	Axis Jet	180 km	

The cavity formed by an asteroid impact on the moon is strongly dependent upon the strength characteristics of the moon rock and whether it is described as a solid with strength or a fluid without strength. With sufficient strength the cavity grows to a maximum size and no axis jet is formed. The size of the cavity is strongly dependent upon the density of the asteroid and its velocity. The initial impact pressures and temperatures are well above shock melting conditions at the impact surface of the moon. The impact pressure for the basalt projectile is greater than 1 megabar, the impact density is greater than 5 g/cc, and the impact temperature is greater than 6000 K. The initial impact pressure for the iron projectile is greater than 1.5 megabar and the iron impact density is greater than 11 grams/cc.

Soon after the initial impact and the cavity formation is occurring, the previously shocked and compressed rock is being rarefied and pulverized. The rock is called “fluidized” and modeled as described in the modeling of crater formation of the Arizona meteor crater and the SEDAN nuclear crater.



Mare Orientale

NASA, Lunar Orbiter 4

900 km across

Collision caused ripples in the lunar crust resulting in three (5 according to Van Dorn) concentric circular ring like features.

It is relatively unflooded by mare basalts.

The outermost ring is 930 km in diameter with ejecta extending 500 km beyond.

Figure 1. The mare Orientale photographed by Lunar Orbiter 4.

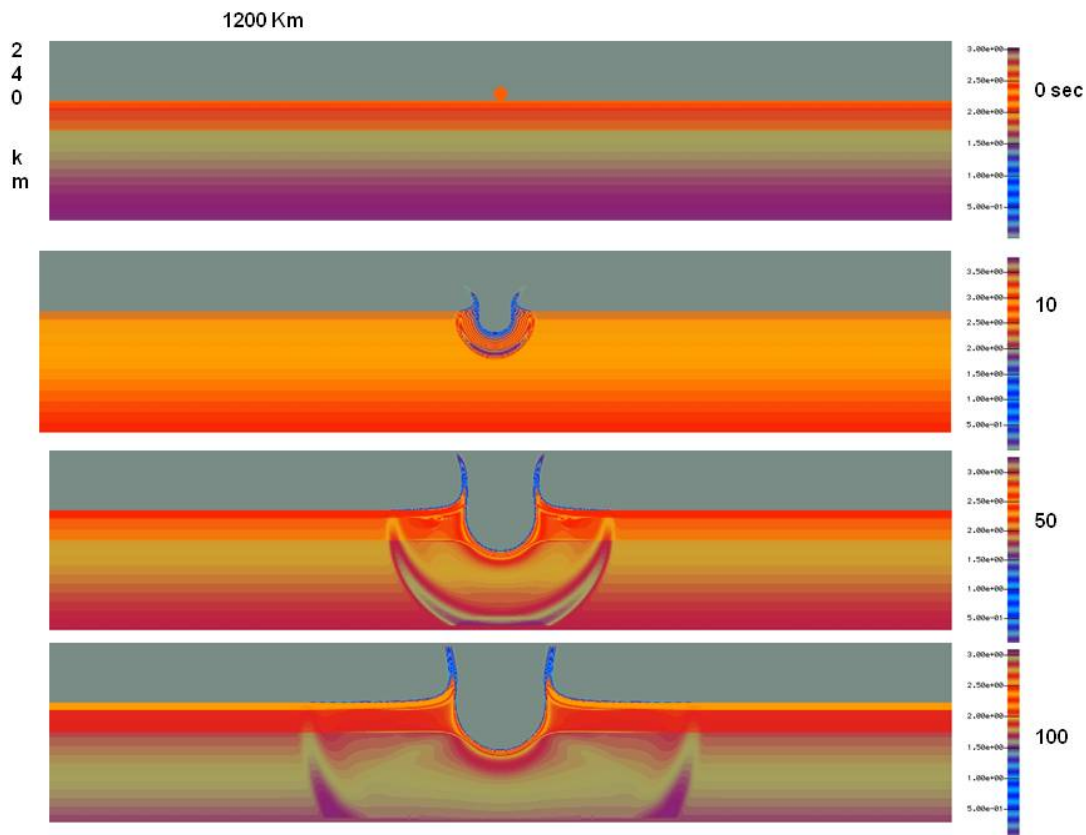
The moon crater formation by an asteroid impact was modeled for a 1200 and 800 kilometer diameter block of Basalt, 160 kilometer thick. Above the Basalt was 80 kilometers of void making the problem 240 kilometers high. The geometry was cylindrical with the projectile impacting on the

cylindrical axis. The gravity constant for the moon used was 167, which compares with 980 for the earth.

MAGNS was used to model the impact of a 10 kilometer diameter Iron Asteroid moving at 10 kilometers/sec with 10 kilometer thick Basalt Crust at 2.86 g/cc, 30 kilometer thick Basalt Mare at 3.10 g/cc and 120 kilometer thick Basalt Mantel at 3.31 g/cc. The basalt yield was 0.01 kilobar. Similar results were obtained for basalt yields up to 0.1 kilobar.

The density contours are shown for the first hour after impact in Figure 2. The times are in seconds. After the moon cavity, rings and mascon have been formed the density, pressure and velocity in the Y direction contours are shown for 800 kilometer diameter in Figure 3 and compared with the Orientale crater in Figure 4 using the Van Dorn locations of the rings.

A PowerPoint and movies are available at www.mccoehi.com/moon/moon.htm .



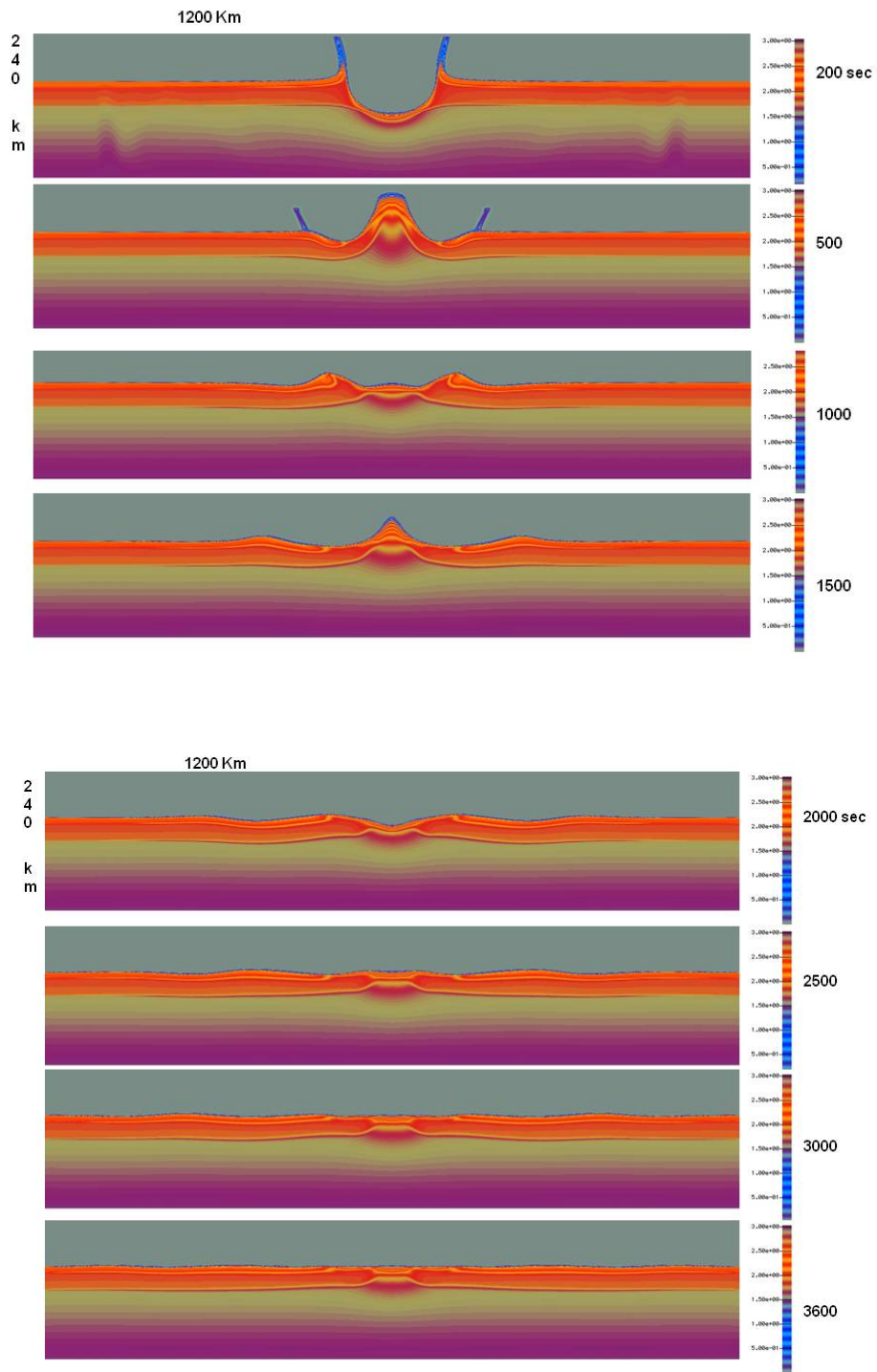


Figure 2. The density contours for a 1200-kilometer diameter block of Basalt impacted by a 10 kilometer diameter Iron Asteroid moving at 10 kilometer/sec.

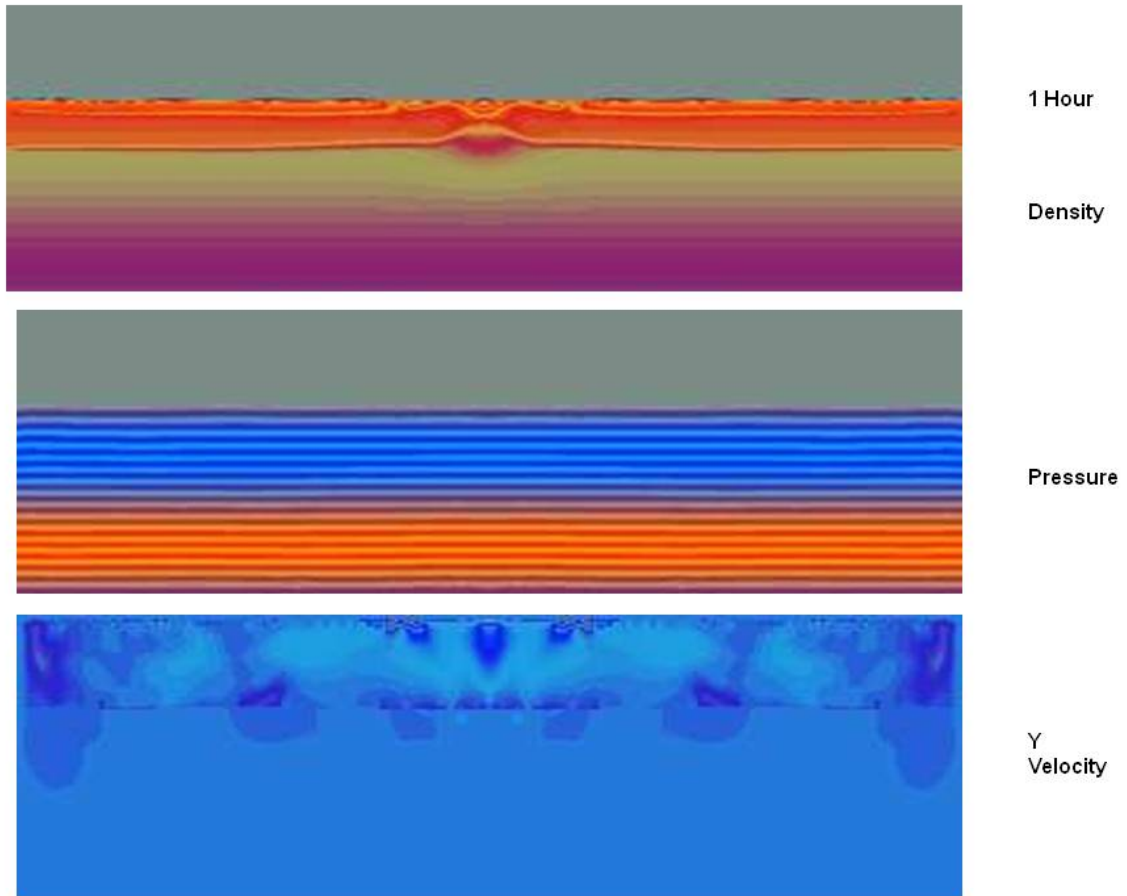
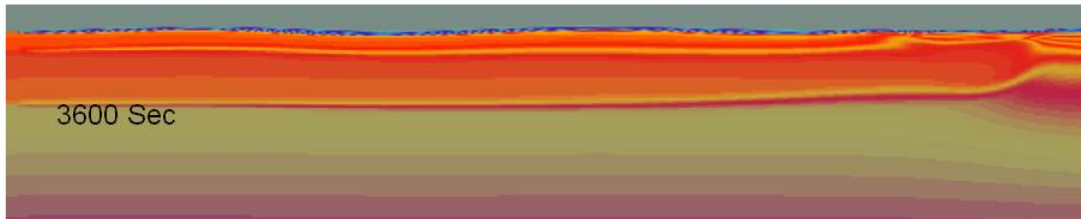


Figure 3. The density, pressure and velocity in the Y direction contours, 3600 seconds after a 800-kilometer diameter block of Basalt is impacted by a 10 kilometer diameter asteroid moving at 10 kilometers/second.

Cavity Diameter - 100 sec 120 km **Orientele 136 km**
 130 130
 At Max Depth 150 140
 200 150 - Cavity Depth Decreasing



0 km Ht	1	-2	1	-1	1	-4	1
595 km	495	380	270	170	115	65	0
	100	115	110	100	65	55	

Orientele Crater Ring Peak Locations and Heights at 62 minutes Freeze Time

680	465	310	240	180
0.5	1.5	3.0	2.5	0.5

Figure 4. The density profile at 3600 seconds for a 600-kilometer radius Basalt block with the height and radius of the calculated maximum and minimum crater rings and distances between the maximum and minimum shown in black. The Van Dorn Orientele peak crater ring locations and heights are shown in red. The calculated maximum crater diameter at various times is shown at the top of the figure.

The number of rings and their locations and heights as determined by Van Dorn are not accurately modeled. Modeling the moon as a flat cylinder instead of a sphere may be a major source of the failure to describe the Orientele rings. The fluidization model and its calibration may also contribute to the failure to describe the Orientele ring number, locations and heights. The number of rings and their location and heights is also difficult to evaluate accurately from the available photographs. The size and velocity of the asteroid is also unknown. The Van Dorn published mechanism for the formation of the rings, his "Tsunamis on the Moon" is supported by the modeling. The tsunami wave occurred in molten and pulverized rock instead of water.

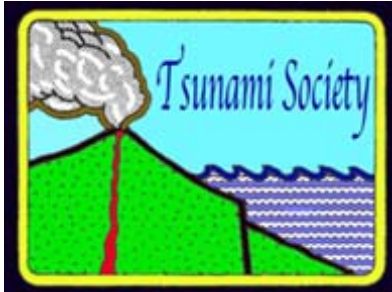
ACKNOWLEDGMENTS

The contributions of Dr. William Van Dorn, Dr. Rob Coker and Dr. Galen Gisler are gratefully acknowledged.

REFERENCES

1. Van Dorn, W., 1968, Tsunamis on the Moon?. *Nature*, v. 220, No. 5172, p. 1102-1107.
2. Van Dorn, W., 1969, Lunar Mare Structure and Evolution. *Science*, v. 165, p. 603-695.
3. Mader, C.L., 2004, **Numerical Modeling of Water Waves- Second Edition**, CRC Press, Boca Raton, Florida.
4. Mader, C.L., 1998, **Numerical Modeling of Explosives and Propellants**, CRC Press, Boca Raton, Florida.
5. Gittings, M.L., 1992, SAIC's Adaptive Grid Eulerian Code, Defense Nuclear Agency Numerical Methods Symposium, p. 28-30.
6. Holmes, R.L., Dimonte, G., Fryxell, B., Gittings, M.L., Grove, J.W. Schneider, M., Sharp, D.H., Velikovich, A.L., Weaver, R.P., and Zhang, Q., 1999, Richtmyer-Meshkov Instability Growth: Experiment, Simulation and Theory, *Journal of Fluid Mechanics*, v. 9, p. 55-79.
7. Baltrusaitis, R.M., Gittings, M.L., Weaver, R.P., Benjamin, R.F., and Budzinski, J.M., 1996, Simulation of Shock-Generated Instabilities, *Physics of Fluids*, v. 8, p. 2471-2483.
8. Mader, C.L., 1999, Modeling the 1958 Lituya Bay Tsunami, *Science of Tsunami Hazards*, v. 17, p. 57-67.
9. Mader, C.L., 2002, Modeling the 1958 Lituya Bay Mega-Tsunami, II, *Science of Tsunami Hazards*, v. 20, p. 241-250.
10. Mader, C.L., and Gittings, M.L., 2003, Dynamics of Water Cavity Generation, *Science of Tsunami Hazards*, v. 21, p. 91-118.
11. Gisler, G., Weaver, R., Gittings, M.L. and Mader, C., 2003, Two- and Three-Dimensional Simulations of Asteroid Ocean Impacts, *Science of Tsunami Hazards*, v. 21, p. 119-134.

12. Gislser, G., Weaver, R., Gittings, M.L. and Mader, C., 2004, Two- and Three-Dimensional Asteroid Impact Simulations, Computers in Science and Engineering.
13. Charles L. Mader, C.L., 2009, Numerical Modeling of Crater Formation by Meteorite Impact and Nuclear Explosion, PREDICTIVE MODELING OF DYNAMIC PROCESSES, p. 447-457, Springer.
14. Mader, C.L. and Michael Gittings, M., 2004, Numerical Modeling of Oblique Initiation of Insensitive High Explosives, www.mccohi.com/oblique/oblique.htm.



SIMULATION OF SCOURING AROUND A VERTICAL CYLINDER DUE TO TSUNAMI

Kuswandi¹, Radiana Triatmadja^{2*}, Istiarto²

¹PhD Student, Department of Civil and Environment Engineering, Faculty of Engineering, Universitas Gadjah Mada, Indonesia

²Department of Civil and Environmental Engineering, Faculty of Engineering, Universitas Gadjah Mada, Indonesia.

^{1,2}Member of Tsunami Research Group, Universitas Gadjah Mada, Indonesia

* Corresponding author radiana@ugm.ac.id

ABSTRACT

Local scour due to tsunami is damaging especially on shallow foundation. Although relatively in a short duration, tsunami attack may scour material around buildings that led to destruction. A number of formulae on local scouring due to flood and tsunami have been available. The local scouring pattern and depth produced by tsunami may be affected by tsunami duration and tsunami surge Froude number and hence different to that resulted by flood which normally have much longer duration and lower Froude number. The research used a relatively short flume to create short duration tsunami surge that run-up on 1:20 beach slope and hit a vertical cylinder on land. Both the pattern and the depth of local scouring around the cylinder were observed and the results were compared with similar research but with different tsunami surge characteristic. It was shown that the maximum scour depth was significantly deeper than the final scour depth. When compared with other experimental study of local scour due to tsunami, the present local scour maximum depth seemed to be slightly less. This could have been caused by the relatively short duration of the present experiment. It was also found that the sidewall effect was insignificant when the ratio of cylinder diameter to the flume width was less than approximately 0.15.

Keywords: *Tsunami, scouring, maximum depth, numerical model, physical model, dam break*

1. INTRODUCTION

Scouring due to tsunami or floods may undermined structure stability and cause further structure failure. Triatmadja, et al (2011), FEMA (2007), Tonkin et al. (2003) and Jain et al, (1979), have showed many examples of scouring around structures. The scouring around cylinder especially bridge piers have been studied and relatively simple formulas for predicting such scouring have been established. These are for example as provided in Table 1. It can be seen from Table 1 that in general, the maximum scouring depends on a number of parameters these are Froude number (water depth and flow velocity), cylinder diameter, and sediment material. The duration is missing in many of the formula since most of the study was conducted for river flow where the duration may be long enough to create the maximum scouring depth irrespective of the duration. Naturally the maximum scouring depth dependent on the natural slope of repose of the material, since whenever the scour depth around the cylinder created a slope that larger than the angle of repose, the bed material slide down to create a stable slope and buried the scour hole.

Table 1. Maximum scouring around a vertical cylinder

Author(s)	Formula	Parameters used	Caused	Equation
Triatmadja, et al (2011)	$d_s/d_0 = 0.25 \text{ to } 0.3$	d_0	Tsunami	(1)
Dames and Moore(1980)	$d_s/h_0 = 0.4$	h_0	Tsunami	(2)
Tonkin (2003)	$d_s = \frac{\Delta P}{\gamma_b \Lambda} \left(1 - 4i^2 \operatorname{erf} \left[\frac{d_s}{2\sqrt{c_v \Delta T}} \right] \right)$	Λ, P, c_v	Tsunami	(3)
Jain et al (1979)	$d_s/b = 2.0(F_r - F_c)^{0.25} (d/b)^{0.8}$	F_r	Floods	(4)
CSU (1992)	$d_s = 2.0 K_i d F_r^{0.43} \left(\frac{b}{d} \right)^{0.65}$	F_r, b, d	Floods	(5)

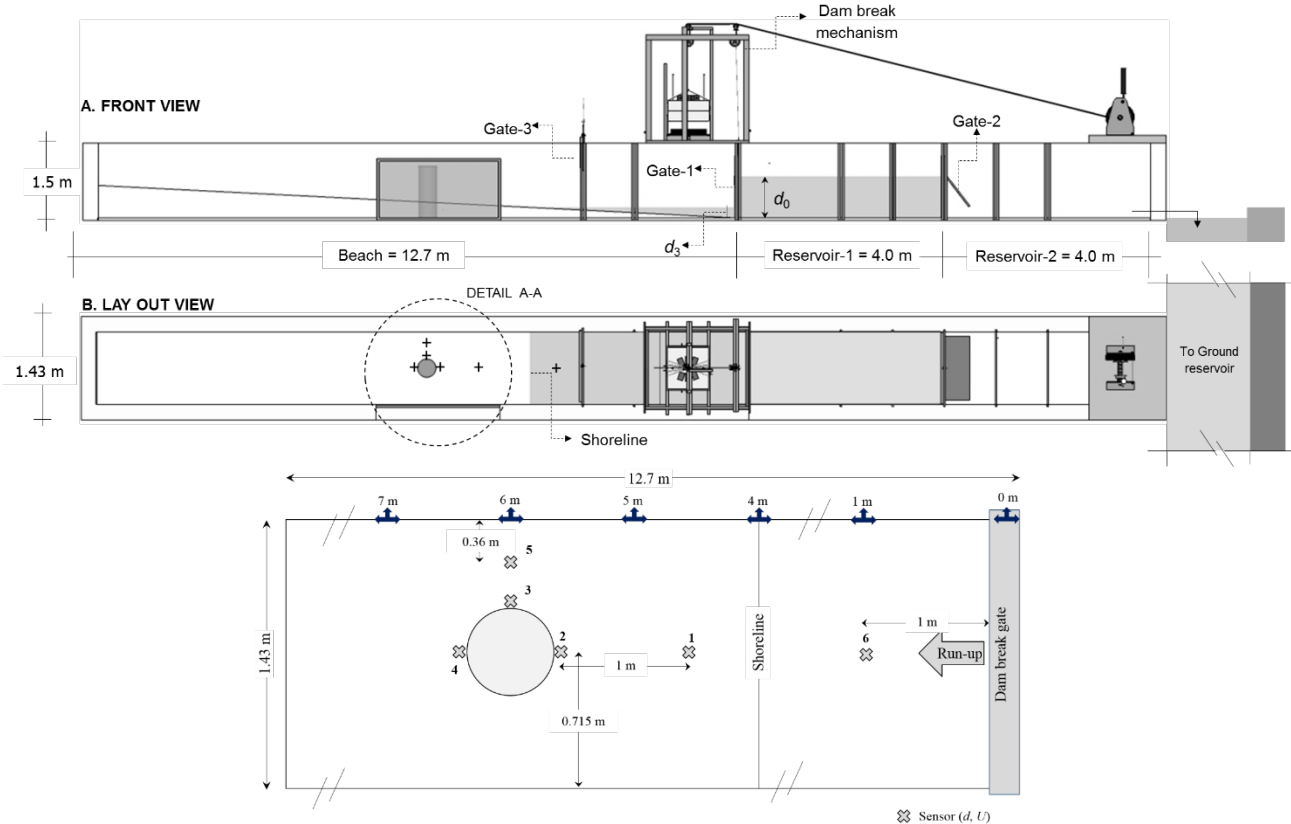
d_s: maximum scouring, *d₀*: water depth of the reservoir, *h₀*: tsunami height, *b*: width or diameter of cylinder, *d*: water depth at the location of the building, *F_r*: Froude number, *F_c*: critical Froude number, *P*: pore pressure, *Λ*: a scour enhancement parameter, *ΔT*: time scale, *C_v*: Terzaghi's coefficient of consolidation, *K_i*: correction factor

The local scour process may be slightly different during tsunami attack. Tsunami may last (starting from run-up up to the end of run-down) only a few hours hour or even only a few minutes. The run-up duration is more or less the same as the run-down duration. In between the run-up and run-down processes there is time when the velocity is nearly zero normally at maximum inundation. Another difference between tsunami scour and river flood scour is the speed and the Froude number of the flow. Tsunami surge flow is significantly faster than the river flood. Other than that, the Froude number of the surge is normally higher especially near the coastline. The difference of speed and Froude number may create different pattern of scouring and maximum scouring depth. The run-down has different flow pattern than the run-up. Such different flow pattern is expected to yield different scouring pattern created by tsunami during run-up.

The study is aimed at finding the local scour depth around a vertical cylinder due to tsunami attack based on physical simulations using dam break surge to represent tsunami.

2. Materials and Method

A model of coastal zone was prepared in a flume of 20.7 m long (L), 1.45 m wide (B), and 1.5 m high (h) (Figure 1). From downstream end of the flume to 12.7 m upstream, the flume bed was sloping with a ratio of 1:20 (vertical: horizontal). About 11.7 m of it was made of fine sand, which represented erodible sandy beach. Two quick opening gates were installed. The first was at 12.7 m from downstream end of the flume, the other was 4 m upstream of the first. In between the gates water were initially stored to generate tsunami like surge by opening the two gates at the same time quickly. Kuswandi et al (2017) have employed this method. The resulting surge was a tsunami like surge that run-up on land (downstream) and another surge that went directly to the ground tank to reduce the effect of secondary run-up. The surge height was varied by varying the water depth in the reservoir (d_0) and the water depth at downstream of the first gate (d_3). The depth of the water downstream of the first gate varied due to the bed slope. The difference between initial upstream water depth or the initial reservoir water depth (d_0) and the downstream water depth d_3 is d' . The maximum height of the surge is $d'' = 4/9 (d_0 - d_3)$ which occurred at the location of the first gate.



B. Detail A-A Figure 1. Experiment setup (Kuswandi, et al., 2017)

A number of tests to observe the scouring pattern around a vertical cylinder were conducted as listed in Table 2. The diameter of the vertical cylinder (b) was also varied to observe its effect on the surge flow pattern and the resulted local scour. As can be expected a large relative cylinder diameter (b/B) may obstruct the flow and even create backwater. This change of pattern may subsequently change the scouring pattern around the vertical cylinder. Four cylinder diameters were to be tested. These were $b/B = 0.07$, $b/B = 0.14$, $b/B = 0.25$ and $b/B = 0.35$. After each test, the scour and erosion was filled with bed sediment (sand) to obtain a smooth slope.

Table 2. List of the simulations

Test	d_0	d_3	$d' (m)$	b/B	Test	d_0	d_3	$d' (m)$	b/B
1	0.45	0.18	0.27	0.07	7	0.45	0.18	0.27	0.25
2	0.50	0.20	0.30		8	0.50	0.20	0.30	
3	0.55	0.22	0.33		9	0.55	0.22	0.33	
4	0.45	0.18	0.27	0.14	10	0.45	0.18	0.27	0.35
5	0.50	0.20	0.30		11	0.50	0.20	0.30	
6	0.55	0.22	0.33		12	0.55	0.22	0.33	

d_0 is the reservoir water depth, d_3 is downstream depth, $d' = d_0 - d_3$

The measurement of the scour was conducted using a laser distance meter after the run down was completed and no water was inside the scour hole. The area that has been scoured may also be filled by sediment during the process of run-up and run-down, when the velocity of the flow reduced significantly. In order to observe the maximum scour depth, a simple tool was installed at certain locations. The tool was a wire mesh of 1 cm square opening, which was shaped like a cylinder and was installed vertical at the location of the study (Figure 2). Most part of the wire mesh was under the sediment surface and only a few portions was above the sediment bed and above the glass ball to make sure that the glass ball stayed inside the wire mesh during the simulation. Other than that, before implemented, the method was tested a number of time to assure that there was insignificant local scouring due to the wire mesh itself.

It was expected that when the maximum scour depth occurred, the ball fell at the lowest elevation. Whenever re-deposition occurred later, the ball would still be at the lowest position but was covered by sediment. In this way, the maximum scour depth can be observed.

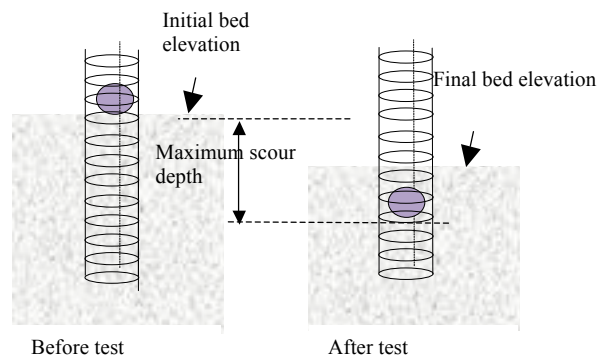


Figure 2. Example of glass ball positions within the cylinder mesh before and after the experiment.

The bed material was of very fine sand where the particle size distribution is provided in Figure 3. As can be seen that most of the sand diameters were between 0.1 mm and 0.4 mm with mean diameter equals 0.19 mm. Hence, the material may be classified as fine sand. Other characteristics values of the bed material are given in Table 3. The sediment porosity was quite high whilst the density was less than 2.0 ton/m³.

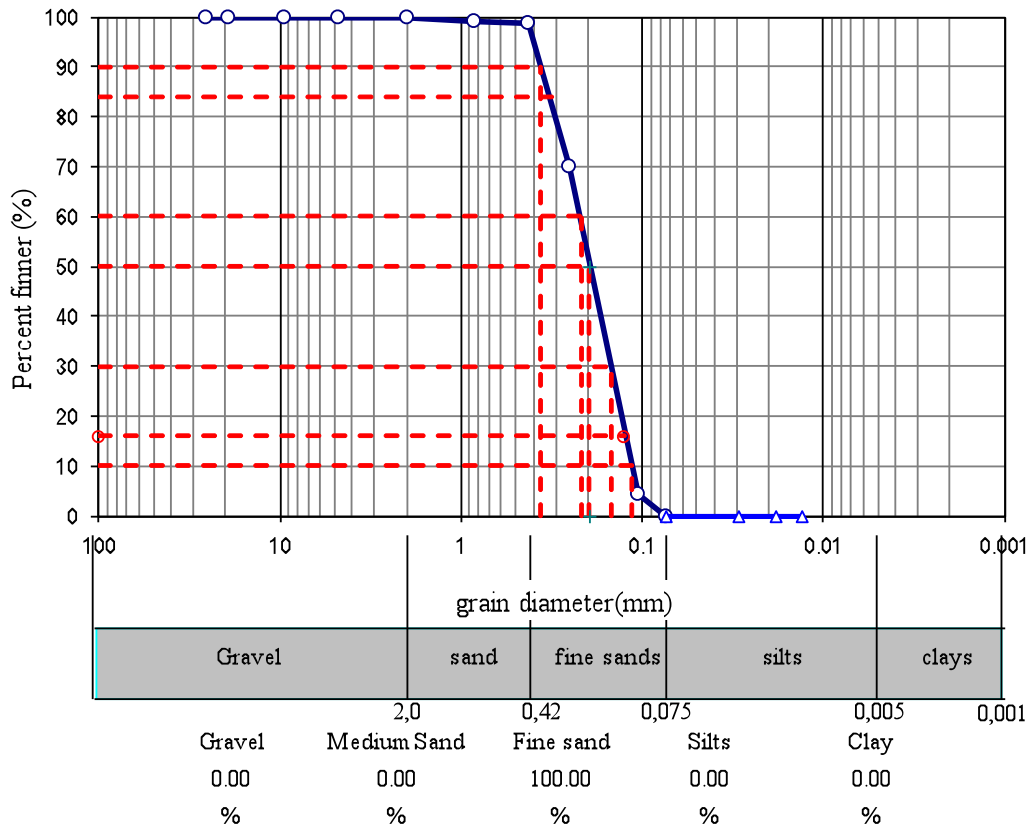


Figure 3. Grain sizes distribution of the sediment bed

Table 3. Characteristics of bed material, Kuswandi et al, (2017)

Properties	Value
diameter (d_{50})	0.19 mm
ρ_s	1.76 ton/m ³
porosity	0.45
average fall velocity	4.9 cm/s

3. Experimental results

1. Effect of relative cylinder diameter

As has been discussed above that the sidewalls may significantly affect the flow pattern when b/B was significantly large. Figure 4 provides a clear indication of the effect of the sidewalls during run-up at different value of b/B .

At time $t = 0.53$ seconds where the surge front just hit the cylinder (see Figure 4, top), all pictures show that there was no sidewall effect. As can be seen the water levels at the wall were almost the same for all model. There was no effect of sidewalls on the simulation (Figure 4, center) even after the surge hit the cylinder for 0.12 seconds. However, the reflected wave from the cylinder start to move toward the walls. Triatmadja and Nurhasanah (2012) used the same dam break system and flume and found that the reflected wave from the center of the flume required less than 0.5 seconds to reach the walls.

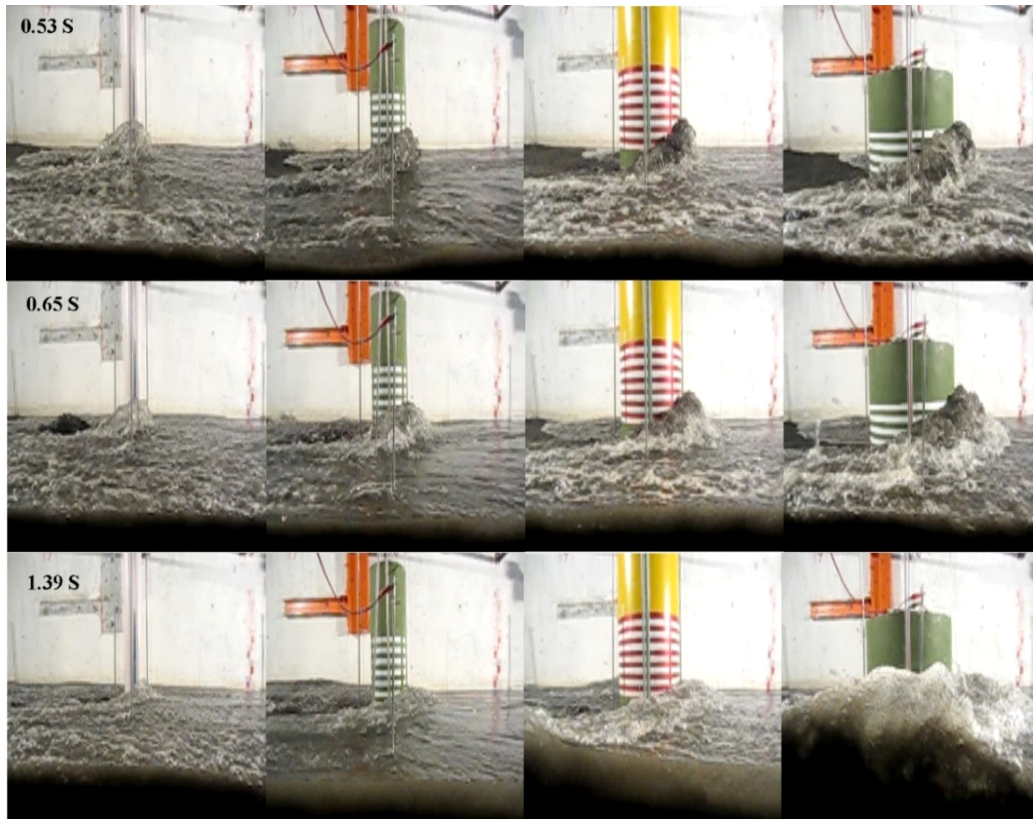


Figure 4. Sidewalls effect

At 1.39 seconds or about 0.86 seconds after the surge hit the cylinder, the effect of the cylinder on the flow pattern become obvious. The largest value of $b/B = 0.35$ resulted in a significant backwater as can be seen at the wall (Figure 4 bottom right). The difference of water level at the same observation time with $b/B = 0.25$ clearly indicated that the diameter of cylinder was too large to be free of sidewalls effect. The relative cylinder diameter of $b/B = 0.14$ and $b/B = 0.07$ showed no effect on the sidewall at the same observation time. This concludes that the relative cylinder diameter that can be used without any sidewalls effect is less than 0.15. Kato et al. (2000), mentioned that their simulation using relative cylinder diameter of $b/B = 0.25$ did not significantly affect the run-up height and hence they concluded that such relative cylinder diameter may be

used to study local scouring around cylinder. Tonkin et al. (2003) who used the same relative cylinder diameter, made similar claim because the local scour extended less than half way between the sidewall and the cylinder. In their cases however, the tsunami were represented by solitary wave that has not broken prior to hitting the cylinder. It may be expected that the flow velocity at the cylinder location be significantly smaller compared to the present study. Hence, the effect of the relative cylinder diameter could have been more tolerated.

2. Scouring around a vertical cylinder

The simulation of scouring around a vertical cylinder was conducted only for $b/B = 0.14$ and 0.07 as these cylinders were relatively small and no sidewalls effect was observed. The results of the scouring patterns were given in Figure 5 up to Figure 8. When the relative cylinder diameter was large (0.14), the scouring pattern was not symmetrical around the cylinder (Figure 5 and 7). These results were different compare to that of Tonkin, et al (2003). As mentioned previously, the different of flow speed and Froude number could have some contribution to the difference. The present experiment produced significantly less scouring depth at both the upstream and the downstream of the cylinder. However for $b/B = 0.07$ the scour pattern was almost symmetrical (Figure 6 and 8). As can be seen more clearly in Figure 8 that the cross section along the shore (from left to right) and the cross section across the shore (front to back) were similar. This result was closer to that of Tonkin, et al (2003). As mentioned in the previous chapter that the wall effect was relatively small or negligible during the experiment with $b/B = 0.07$. Secondly, as the cylinder was small, the effect of separation flow only last for relatively short duration.

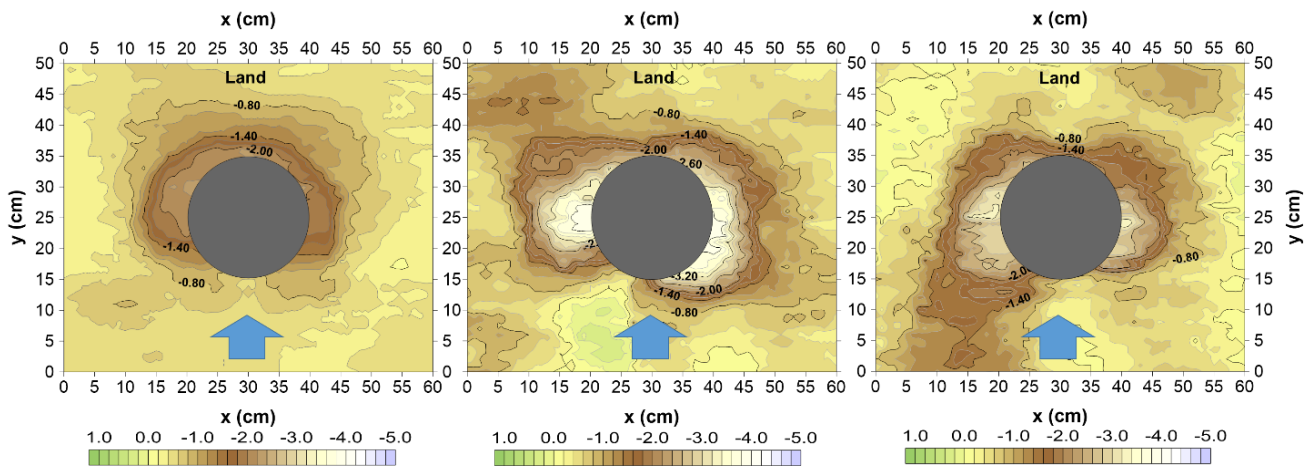


Figure 5. Scouring pattern around cylinder ($b/B = 0.14$) with $d' = 0.33$, $d' = 0.30$, $d' = 0.27$ respectively

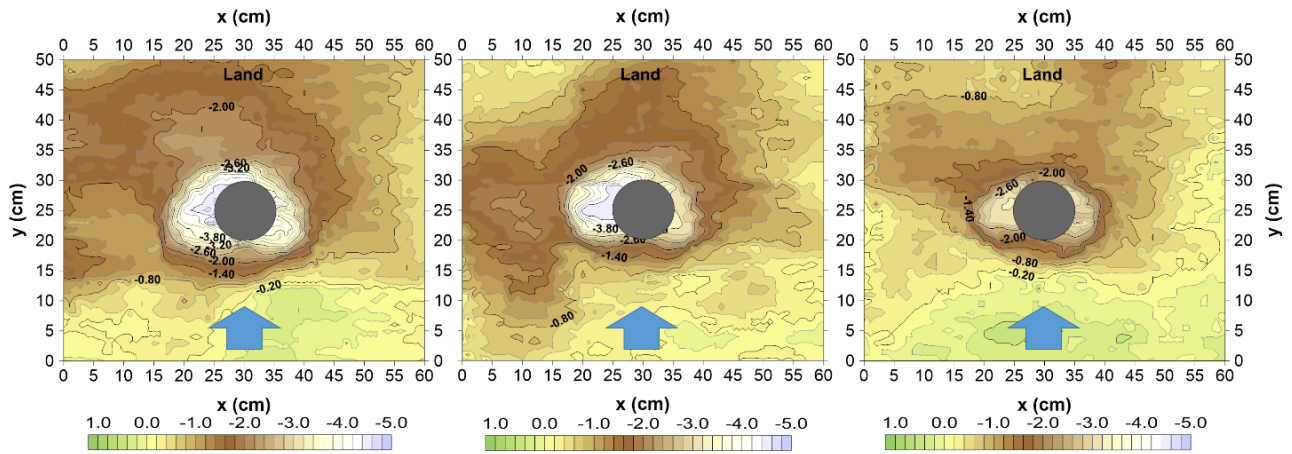


Figure 6. Scouring pattern around cylinder ($b/B = 0.07$) with $d' = 0.33$, $d' = 0.30$, $d' = 0.27$ respectively

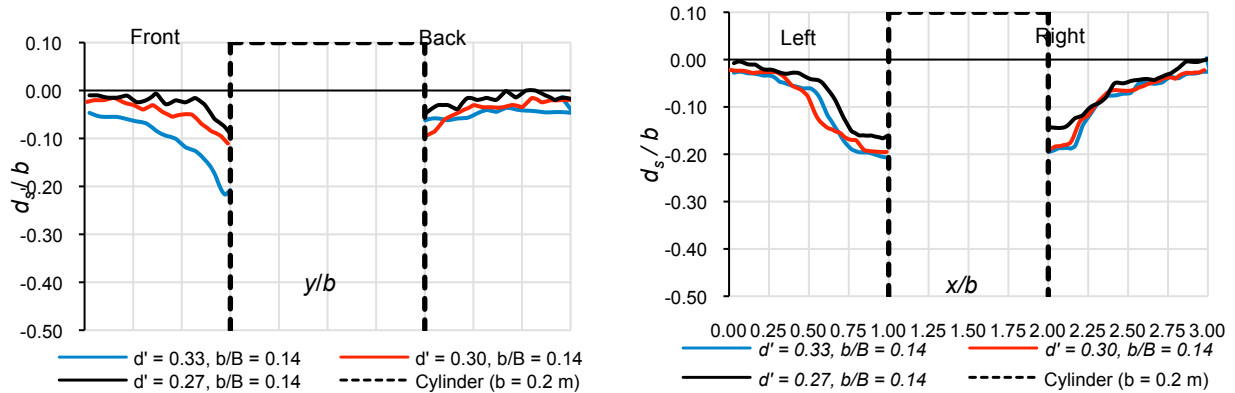


Figure 7. Cross and long sections of scouring at $b/B = 0.14$

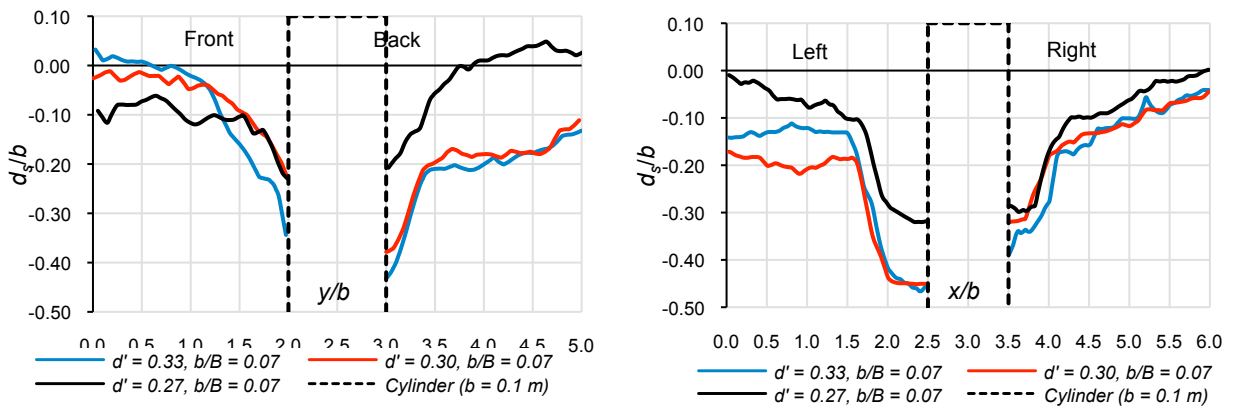


Figure 8. Cross and long sections of scouring at $b/B = 0.07$

3. Maximum scouring depth

The maximum scouring depth for each experiment was plot in Figure 9. The figure indicates clearly that the maximum scour depth were deeper than the final scour depth d_s . In average, the maximum scour was 1.5 times of the final scour depth.

It seems that the scour depths were independent of b or the cylinder diameter as also was found by Triatmadja et al. (2011). The final scour depth ranged from $0.27 d''$ to $0.34 d''$ whilst the maximum scour ranged from $0.35 d''$ to $0.60 d''$. It may be said that

$$dsd''=0.34 \quad (6)$$

$$dsmaxd''=0.60 \quad (7)$$

Where d_{smax} is the maximal scour depth. Equation 7 is comparable to Equation 1 of Triatmadja et al (2011). The value of d'' in this experiment was equal to $4/9(d_0)$ in Triatmadja's and hence based on Equation 1,

$$0,56 \leq dsd'' \leq 0.67 \quad (8)$$

Although they only observed the final scour depth but since their experiment employed horizontal slope, no run-down occurred and less re-deposition occurred in the scour hole was expected. The result of the present experiment is in between the range given by Triatmadja et al. (2011).

The maximum scour depth of the present experiment can also be presented in term of the maximum flow depth. Unfortunately, no observation was conducted to obtain the data across the shore. However the water depth at 1 m or $6.8 d''$ in front of the cylinder was recorded. This location was approximately 1 m or $6.8 d''$ downstream of the coastline. Hence the data at this location was used to represent the maximum flow depth (d_{max}) to yield $dsdmax= 0.63$. Dames and Moore (1980) as reported by FEMA suggested that the approximated maximum scour for loose sand was $dsdmax= 0.6$ at a distance greater than 300 ft and $dsdmax= 0.8$ at a distance less than 300 ft (approximately 91 m). Considering that the maximum d'' or tsunami height in the present experiment was 0.15 m, it may be said that the scale of the present model was more or less 1:100 depending on the real tsunami height. With a 1:100 scale model the distance of the cylinder from the coastlines was approximately 50 m in which $dsdmax = 0.80$. The present maximum scour therefore was 0.80 of the approximated scour depth by Dames and Moore (1980). Similarly the maximum scour obtained by Tonkin et al (2003) was presented based on the maximum tsunami flow depth by the present authors to yield $dsdmax = 0.91$ which was slightly larger than 0.80 as suggested by Dames and Moore (1980).

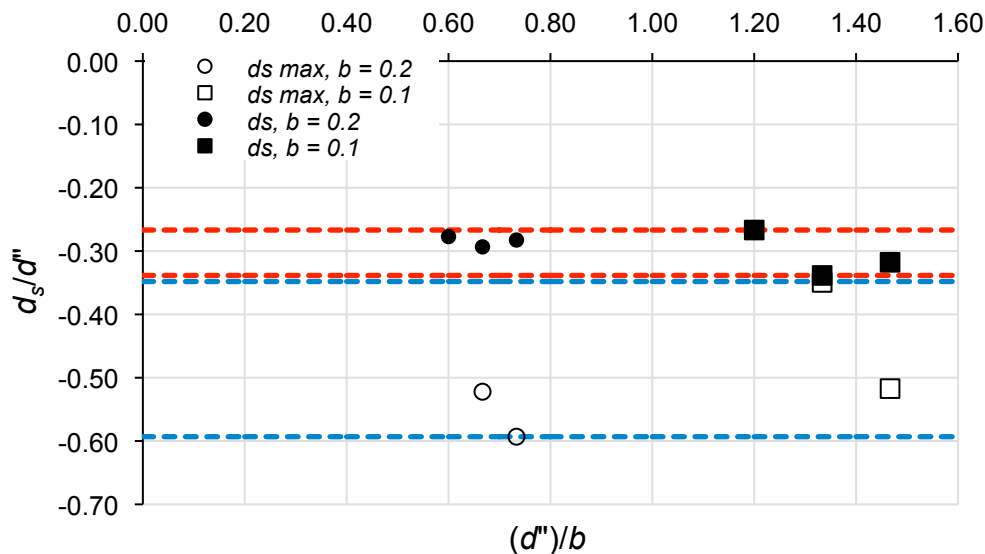


Figure 9. Final and maximum scour depth around cylinder due to relatively short tsunami

3. Conclusion

1. The maximum ratio of cylinder diameter to the channel width that may not produce sidewalls effect of tsunami surge model is $(b/B) < 0.15$
2. The maximum local scour around a vertical cylinder during tsunami attack is higher than the final scour due to re-deposition of sediment.
3. The maximum local scour around a vertical cylinder during a tsunami attack may reach approximately 0.60 of the tsunami height. This finding was based on short tsunami. A longer tsunami may result in deeper local scour.

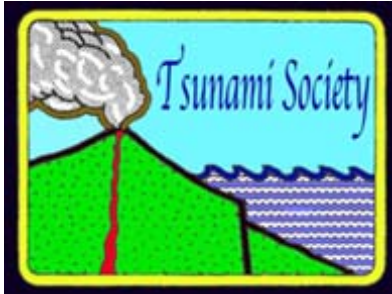
Acknowledgement

The authors thank the government of Indonesia that have provided part of the funding through HIBAH BERSAING research funding scheme.

4. References

- Dames and Moore. Design and Construction Standards for Residential Construction in Tsunami-Prone Areas in Hawaii, prepared by Dames & Moore for the Federal Emergency Management Agency, Washington D.C. , 1980.
- Federal Emergency Management Agency (FEMA). Guidelines for Design of Structures for Vertical Evacuation from Tsunamis. National Tsunami Hazard Mitigation Program. June 2008.
- Jain. C. Subhash and Edward E. Fischer. Scour around Circular Bridges Piers at High Froude Numbers. IIHR report Number 220. The University of Iowa, 1979.

- Kuswandi, Triatmadja. R., and Istiarto. 2017. Simulation of Tsunami Run-up and Scouring around a Vertical cylinder using a Flume of Limited Length. *Indian Journal of Science and Technology*. 2017 (Submitted)
- Kato, F., Shinji, S. & Harry Yeh. Larges-Scale Experiment on Dynamic Response of Sand Bed around a Cylinder due to Tsunami. *Journal Coastal Engineering*, 2000, pp. 1848-1859. ©ASCE DOI: 10.1061/40549(276)144
- Rijn, L. C. Sediment Transport, Part I: Bed Load Transport. *Journal Hydraulic Engineering*, Vol. 110, No. 10. (1984), pp. 1431-1456. ©ASCE, ISSN: 0733-9429/84/0010-1431
- Synolakis, C. E. The Run up of Solitary Waves. *Journal of Fluid Mechanics*, Vol. 185 (1987), pp. 523-546. © Cambridge University Press. DOI: 10.1017/S002211208700329X.
- Tonkin P Susan, Harry Yeh, Fuminori Kato and Shinji Sato. Tsunami Scour around a Cylinder. *Journal Fluid Mechanics*, Vol. 496. (2003), pp. 165-192. © Cambridge University Press. DOI: 10.1017/S0022112003006402.
- Triatmadja. R, S. N. Hijjah and A. Nurhasanah. Scouring Around Coastal Structures Due to Tsunami Surge in 6th Annual International Workshop & Expo on Sumatera Tsunami Disaster & Recovery 2011 in Conjunction with 4th South China Sea Tsunami Workshop, 2011
- Triatmadja. R., and Nurhasanah. A. Tsunami Force on Building with Opening and Protection, *Journal of Earthquake and Tsunami* Vol. 6, No. 4 (2012), pp. 1250024-(1-17). © World Scientific. DOI: 10.1142/S1793431112500248



**BENCHMARK SOLUTIONS FOR TSUNAMI WAVE FRONTS AND RAYS.
PART 2: PARABOLIC BOTTOM TOPOGRAPHY**

An. G. Marchuk

*Institute of Computational Mathematics and Mathematical Geophysics, Siberian Division of Russian
Academy of Sciences, Novosibirsk, Russia*

Abstract. In this paper, the kinematics of the tsunami wave ray and the wave front in the area, where the depth increases proportional to the squared distance to the straight shoreline, is studied. The exact analytical solution for the wave-ray trajectory above the parabolic bottom topography has been derived. This solution gives the possibility to determine in the ray approximation the tsunami wave heights in an area with the parabolic bottom topography. The distribution of the wave-height maxima in the area with such a bathymetry is compared to that obtained with a shallow-water model. All the exact solutions obtained can be used for testing numerical algorithms.

Key words: *tsunami propagation, shallow-water equations, wave ray, wave front kinematics*

1. SOME FEATURES OF THE LONG WAVE PROPAGATION

Tsunami waves, usually generated by vertical displacements of large ocean bottom areas, belong to a class of long waves whose length is at least ten times greater than the depth. The propagation of such waves in a deep ocean, where the wave height is usually two orders lower than the depth, is described by a linear system of differential shallow-water equations (Stocker, 1957). The validity of this description has many times been verified in practice. In the one-dimensional case without external forces (except for the gravity) these equations can be written down in the following form:

$$\frac{\partial \eta}{\partial t} + \frac{\partial(Du)}{\partial x} = 0. \quad (1.2)$$

Here u is the horizontal water flow velocity in the wave, η is the water surface height above an unperturbed level, g is the acceleration of gravity, and D is the depth. It follows from the shallow-water equations that the wave velocity does not depend on its length, and is determined by the Lagrange formula (Stocker, 1957):

$$c = \sqrt{gD}. \quad (1.3)$$

This formula is of fundamental importance for the kinematics of long waves (in particular, tsunamis). For the description the tsunami wave dynamics in the coastal zone, where the tsunami amplitude increases and the depth decreases, the nonlinear shallow water model is used (Marchuk et al., 1983). The wave propagation velocity for this model is expressed by the formula

$$c = \sqrt{g(D+\eta)}. \quad (1.4)$$

For the linear system of shallow water equations the horizontal flow velocity in a moving wave is expressed by the formula (Marchuk, 2016)

$$u = \eta \sqrt{\frac{g}{D}}, \quad (1.5)$$

and for the nonlinear tsunami wave formula (1.5) will be changed to

$$u = \eta \sqrt{\frac{g}{D+\eta}}. \quad (1.6)$$

Independence of the tsunami front propagation velocity on the wave parameters (height and length) gives the possibility for a priori discovery of peculiarities of the wave behavior in areas with uneven bottom. In the paper (Marchuk, 2016) the formula for the 1-D wave height varying in the moving wave has been derived.

In the linear case it can be written as

$$\eta_2(x) \approx \eta_1(x) \sqrt{\frac{D_1}{D_2}}, \quad (1.7)$$

where η_2 and D_2 are the current wave elevation and depth and η_1 and D_1 are the initial values. It is the well-known Green formula describing a height variation of a long wave over an uneven bottom in the one-dimensional case. If a wave front is not straight, the wave amplitude varies not only due to the non-constant depth, but also as a result of wave refraction, that is, the wave-front line transformation. In the same paper (Marchuk, 2016) the relation between the wave segment length and the amplitude of this wave segment was also obtained

$$\eta_2 = \eta_1 \sqrt{\frac{L_1}{L_2}}. \quad (1.8)$$

Here L_2 is the current length of the wave segment and L_1 is its initial length. Thus, due to the cylindrical propagation the tsunami wave height decreases inversely proportional to the square root of the circular front radius or the wave front length. In general, the kinematics of propagation of perturbations in various media is described by the eikonal equation. The governing formulas for the wave-front kinematics are presented in (Romanov, 1984), where the wave ray concept one of whose properties is the orthogonality to the wave-front line at any time is introduced. Along wave rays, a perturbation propagates from a source to other points of the medium in the least time. This means that wave rays are the fastest routes. Between the two closely spaced wave rays (in a ray tube), the wave energy remains constant (Romanov, 1984). Therefore, for a wave segment in a ray tube, formulas (1.7) and (1.8) can be rewritten in the form

$$\eta_2 = \eta_1 \sqrt{\frac{L_1}{L_2}} \sqrt{\frac{D_1}{D_2}}, \quad (1.9)$$

where L_1 and L_2 are the widths of the ray tube (the length of the wave-front line segment inside the ray tube) at the initial and current time moments of wave propagation.

2. EXACT ANALYTICAL FORMULAS FOR WAVE-RAY TRACES ABOVE THE PARABOLIC BOTTOM TOPOGRAPHY

An exact mathematical formula for a wave ray trajectory over a parabolic bottom can be found from the laws of geometrical optics. Let us consider a two-dimensional water area where the depth and the wave propagation velocity vary only in one direction. In this case we can use the Snell law for the wave ray refraction angle in a medium with varying optical conductivity (Sabra, 1981). According to this law, if in a two-dimensional conducting medium a ray comes at the angle of incidence α_1 to the horizontal line (Fig. 2.1), and the conductivity (the propagation velocity of a signal) changes from b_1

to b_2 , then after passing the interface its direction α_2 changes according to the formula

$$\frac{\sin(\alpha_1)}{b_1} = \frac{\sin(\alpha_2)}{b_2}. \quad (2.1)$$

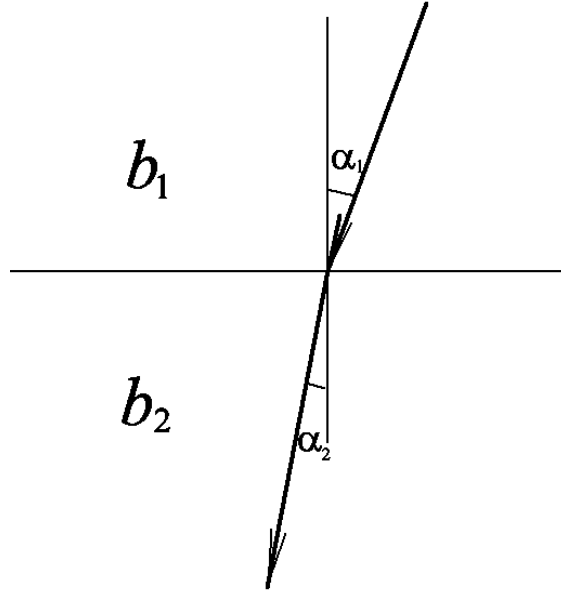


Figure 2.1. Refraction of a wave ray at the interface between two media

Thus, in a medium where the conductivity b (the wave propagation velocity) varies only along one spatial variable (for instance, $b(y)$), the wave ray inclination from the direction of the conductivity gradient α changes according to the formula

$$\frac{\sin(\alpha(y))}{b(y)} = \text{const} = \frac{\sin(\alpha_0)}{b(y_0)}. \quad (2.2)$$

Here α_0 is the initial incidence angle of the wave ray with respect to the vertical at the point $y=y_0$. In the case of a parabolic bottom, where the depth is proportional to the squared medium conductivity $a(y)$ (the tsunami wave propagation velocity) can be determined by Lagrange's formula (1.3), which for a parabolic bottom topography has the following form:

$$a(y) = \sqrt{g \cdot b_1 \cdot y^2} = b_2 \cdot y. \quad (2.3)$$

Here g is the gravity acceleration, y is the distance to the straight coastline where $y=0$, b_1 and b_2 are constant in the whole area. In this case the Snell law (2.2) gives the following wave-ray direction α according to the coastline normal

$$y(\alpha) = b_3 \cdot \sin(\alpha), \quad (2.4)$$

where b_3 is also a constant.

In order to determine the wave ray trajectory above such a bottom topography let us consider the following problem. Let the point $(0, y_0)$ be a starting point for the wave ray that exits this point in parallel to the shoreline direction (Fig. 2.2). At the starting point, the angle $\alpha = \pi/2$. The inclination angle of a wave ray $y(x)$ to the X-axis will be expressed as $\beta = \pi/2 - \alpha$ (Fig. 2.2). Hence, we have

$$\frac{dy}{dx} = \operatorname{tg}(\beta) = \frac{\sin(\beta)}{\cos(\beta)}, \quad 0 < \beta < \pi/2$$

or

$$dx = dy \frac{\cos(\beta)}{\sin(\beta)}. \quad (2.5)$$

From (2.4) and (2.5) follows

$$dx = b_3 \cdot \sin(\beta) \cdot d\beta \frac{\cos(\beta)}{\sin(\beta)} = b_3 \cdot \cos(\beta) \cdot d\beta.$$

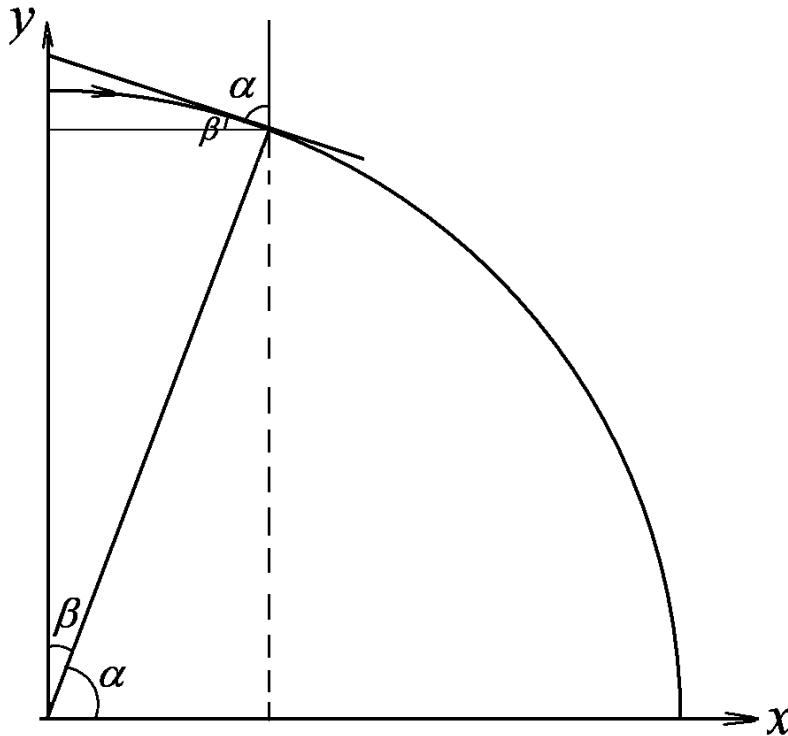


Figure 2.2. The wave ray refraction over the parabolic bottom topography

Assuming that along the wave ray the angle β varies from zero to the positive value β_1 , then after conducting the integration we obtain

$$x = b_3 \cdot \sin(\beta) \Big|_0^{\beta_1} = b_3 \cdot \sin(\beta_1) = b_3 \cdot \cos(\alpha_1), \quad (2.6)$$

where $\alpha_1 = \pi/2 - \beta_1$. In addition to this, as follows from (2.4) for any value of α_1 from the interval $(\pi/2, 0)$

$$y = b_3 \cdot \sin(\alpha_1). \quad (2.7)$$

Formulas (2.6), (2.7) present the parametric equation of the circle of radius b_3 with a center located at the coordinate origin. This radius can be easily determined from (2.4). From this formula it also follows that the circle center is always situated on the X-axis. In the case when the initial wave-ray outgoing direction was in parallel to the shoreline, the circle radius is equal to the offshore distance at this moment. If at some time instance the angle between the ray and the Y-axis is equal to α_0 and the offshore distance at this moment is equal to y_0 , then the radius of the circle which presents the wave ray can be found from (2.4)

$$r = b_3 = \frac{y_0}{\sin(\alpha_0)}. \quad (2.8)$$

If $\alpha_0 = 0$, but at the same time $y_0 > 0$, then the radius will be infinitely big and the ray trajectory will be presented by the straight line which is orthogonal to the coastline.

Unlike the case with a sloping bottom (Marchuk, 2016) here the boundary value problem for a wave ray can be solved without difficulty. Let us have two points (a source and a receiver) (2.3) in the area with the parabolic bottom topography. Let the receiver be situated at the coastline in the coordinate origin $(0, 0)$, and the source coordinates be the following: $x = x_0, y = y_0$. Let, for definiteness, $0 < x_0 < y_0$, which means that a wave ray monotonically approaches the shore (Fig. 2.3).

Taking into account the fact that the wave ray is presented by the circle arc having the center at the shoreline ($y=0$), the unknown radius r can easily be found from the equation of the circle passing the point (x_0, y_0) and the coordinate origin

$$(r - x_0)^2 + y_0^2 = r^2. \quad (2.9)$$

Resolving this equation for the parameter r , the following expression will be written

$$r = \frac{x_0^2 + y_0^2}{2x_0}. \quad (2.10)$$

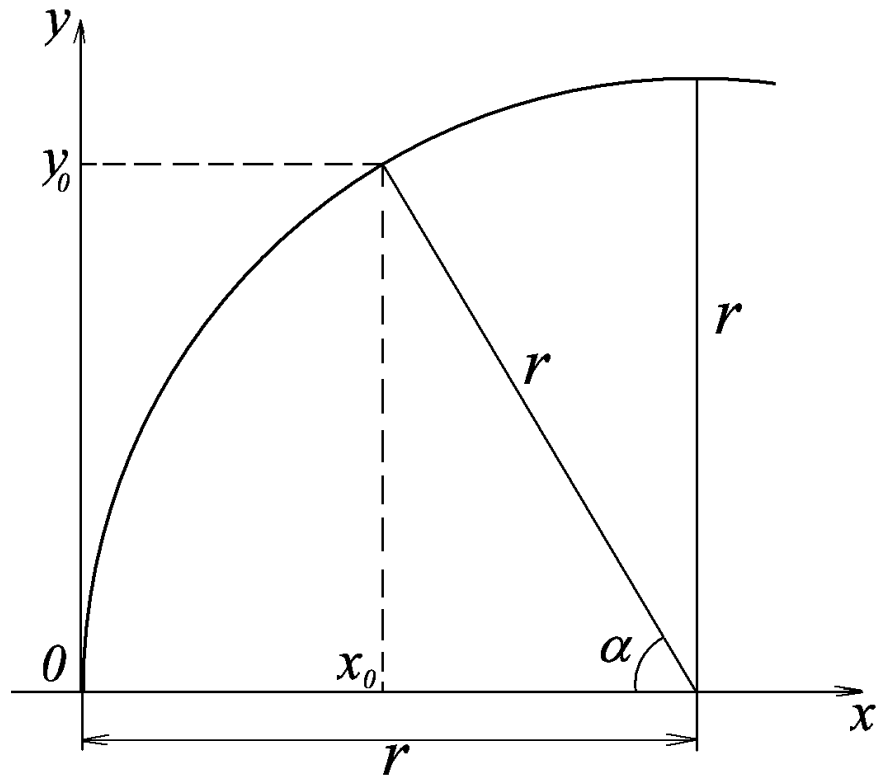


Figure 2.3. The scheme of solving the boundary-value problem for a wave ray above the parabolic bottom topography

Then from the equation of a circle in parametric form

$$(r - x)^2 + y^2 = r^2,$$

the equation of the wave ray passing the point (x_0, y_0) and the coordinate origin can be written down as

$$y = \sqrt{x(2r - x)}, \quad (2.11)$$

where the circle radius r is determined by formula (2.10).

Now with the help of the previously derived formulas let us define the tsunami travel time along the wave ray. Let us consider the wave ray presenting an arc of the circle of radius r with the center located at the point $(x_0, 0)$ (Fig. 2.4). Let initially (when $t=0$) the wave front cross this wave ray at a point **A** with the coordinates (x_1, y_1) . In addition, the segment which connects the point **A** with the center of the circle is inclined at the angle α_1 to the X-axis (Fig. 2.4).

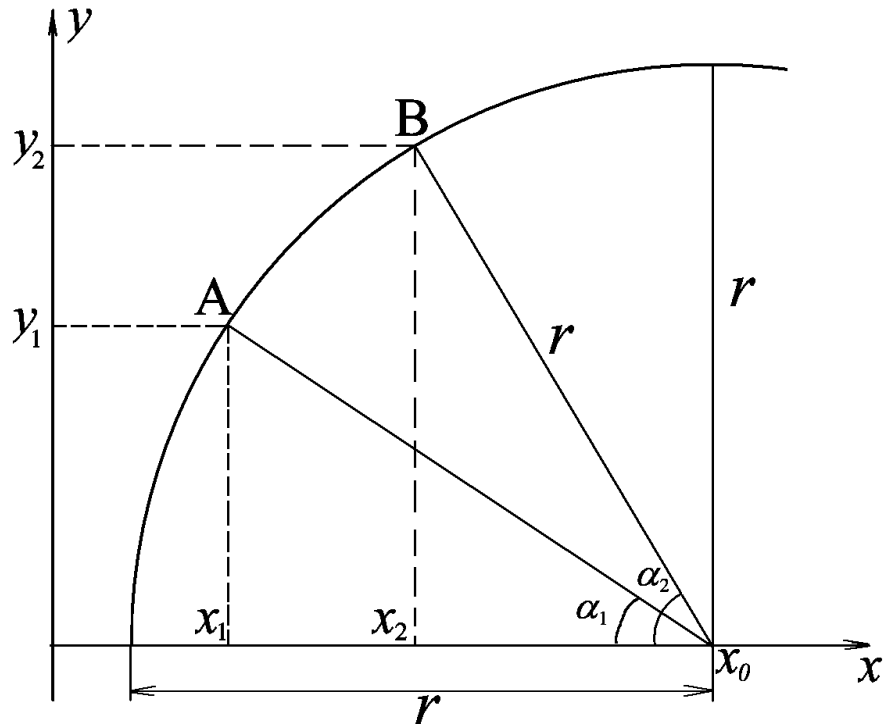


Figure 2.4. The scheme of the travel-time calculation along the wave ray between the points **A** and **B**

Let us find a travel time T which is required for the tsunami wave to arrive at the point **B** with the coordinates (x_2, y_2) and where the radius-vector inclination is equal to α_2 radians. If $0 < \alpha_1 < \alpha_2 \leq \pi$, then with allowance for (1.3) we can express the travel time as the Fermat integral

$$T = \int_{\alpha_1}^{\alpha_2} \frac{d\alpha \cdot r}{\sqrt{gD(x, y)}} \quad (2.12)$$

The depth D all around the area varies according to the formula

$$D(x, y) = k^2 y^2. \quad (2.13)$$

When we come to the variable α , then (2.12) can be rewritten as

$$T = \frac{1}{\sqrt{g}} \int_{\alpha_1}^{\alpha_2} \frac{d\alpha \cdot r}{k \cdot r \cdot \sin(\alpha)} = \frac{1}{k_1} \ln \left| \operatorname{tg} \left(\frac{\alpha}{2} \right) \right|_{\alpha_1}^{\alpha_2} = \frac{1}{k_1} \left(\ln \left| \operatorname{tg} \left(\frac{\alpha_2}{2} \right) \right| - \ln \left| \operatorname{tg} \left(\frac{\alpha_1}{2} \right) \right| \right), \quad (2.14)$$

where $k_1 = k \cdot \sqrt{g}$. The angle α is counted clockwise from the X-axis. From (2.14) it is possible to express the angle α_2 through the angle α_1 and the time T

$$\alpha_2 = 2 \operatorname{arctg} \left(\exp(k_1 T) \cdot \operatorname{tg} \left(\frac{\alpha_1}{2} \right) \right). \quad (2.15)$$

Finally, the coordinates of the destination point which the wave front will reach at the time T going along the wave ray, can be presented as

$$\begin{aligned} x_2(T, \alpha_1) &= x_0 - r \cdot \cos(\alpha_2), \\ y_2(T, \alpha_1) &= r \cdot \sin(\alpha_2). \end{aligned} \quad (2.16)$$

Here α_2 is associated with T and α_1 according to (2.15). If $0 \leq \alpha_2 < \alpha_1 < \pi/2$, then the expression for α_2 (2.15) will be as follows

$$\alpha_2 = 2 \operatorname{arctg} \left(\frac{\operatorname{tg} \left(\frac{\alpha_1}{2} \right)}{\exp(k_1 T)} \right). \quad (2.17)$$

The radius of this circle and its center position are uniquely determined from the source coordinates (x_1, y_1) and the exit angle α_1 of the wave ray (Fig. 2.4)

$$\begin{aligned} r &= y_1 / \sin(\alpha_1), \\ x_0 &= x_1 + r \cdot \cos(\alpha_1) = x_1 + y_1 / \operatorname{tg}(\alpha_1). \end{aligned} \quad (2.18)$$

If $\alpha_1 = \pi/2$, then the radius r is certainly equal to y_1 , and the abscissa of the circle center is the same as the one for the ray exit point (i.e. x_1). Now, using formulas (2.15) and (2.16) it is easy to determine coordinates of the destination point (x_2, y_2) located on the ray, where the wave front arrives at the time instance T .

It follows from formula (2.14) that the travel time is not dependent on the circle radius but only on the sector limits. This means that the travel time along the circle arc between the radius inclination angles α_1 and α_2 (Fig. 2.4) is the same for any concentric circle and the initially straight segment of a wave front will conserve its straight shape in the course of propagation over the parabolic bottom relief. An example of such a behavior of the straight wave front is shown in Figures 2.5 (a)-(d). Here the snapshots of the simulated tsunami wave (the water surface elevation), which propagates off the left boundary of the computational domain, are presented. It is easy to see that the wave front has the straight shape during whole propagation process. Such a property of the initially straight wave front

segment can be used for testing numerical methods for computing the tsunami kinematics and dynamics.

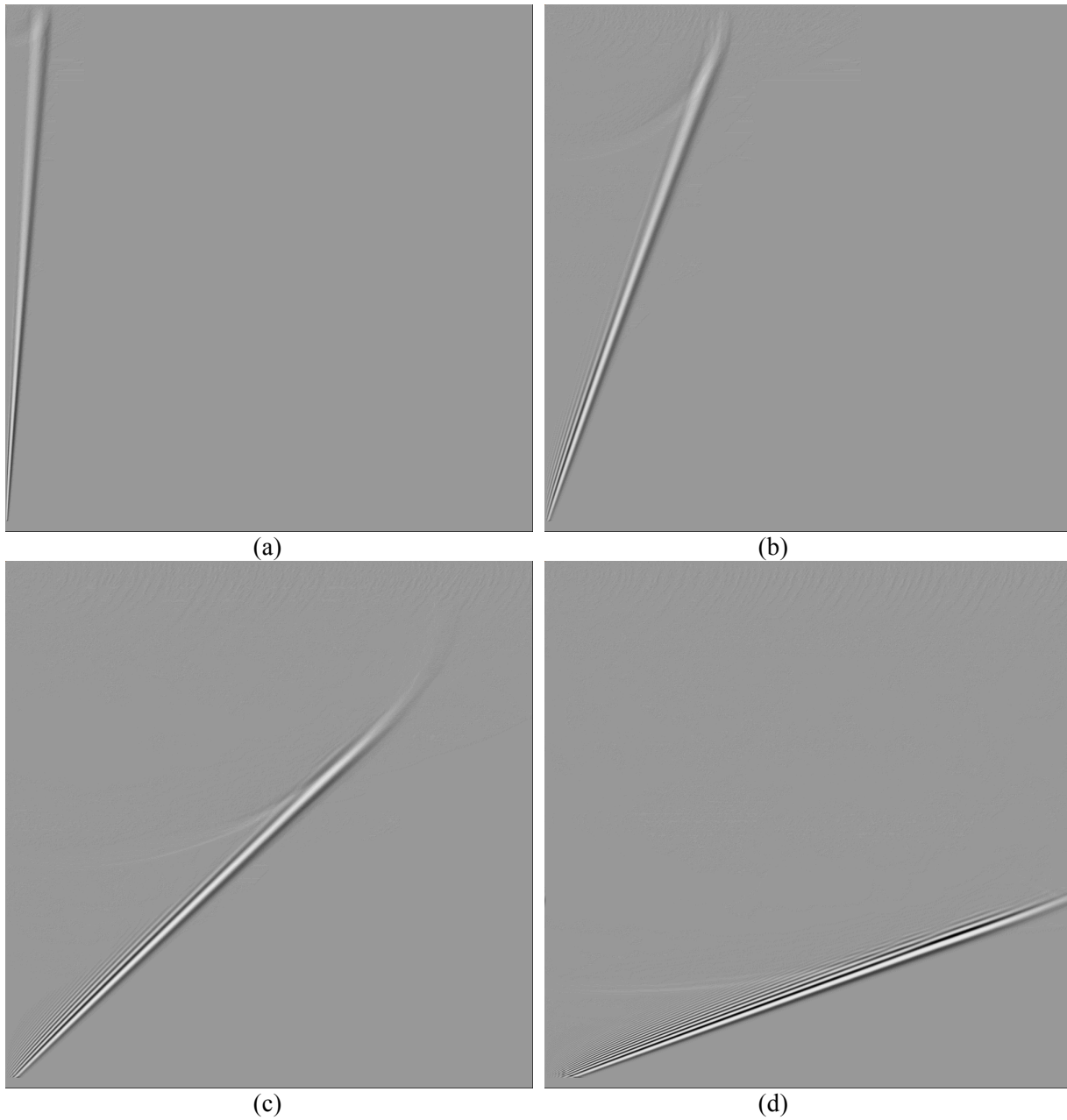


Figure 2.5. The snapshots of the calculated water surface as a result of tsunami propagation off the left boundary.

3. DETERMINATION OF A WAVE-FRONT LINE AND ESTIMATION OF THE WAVE HEIGHT ABOVE THE PARABOLIC BOTTOM

For some model shapes of the bottom, distributions of wave amplitudes (heights) can be found analytically. Consider, for example, the coastal area where the depth increases with a squared distance to the coast with a model tsunami source in the form of a circle of radius R_0 with the center at a distance of y_{00} from a straight coastline. In Figure 3.1, this line coincides with the axis OX ($y = 0$). In Section 2, the wave ray trajectory over a parabolic bottom (as in the case in question) has already been found. In order to determine a tsunami wave height all around the domain with the parabolic bottom topography, let us split it to many ray tubes varying the ray starting points and determining exiting angles there. Then using formulas (2.15) and (2.16) we can find coordinates of the points along each wave ray varying the time parameter T . The ray radius and the abscissa x_0 of the circle center are given by (2.18).

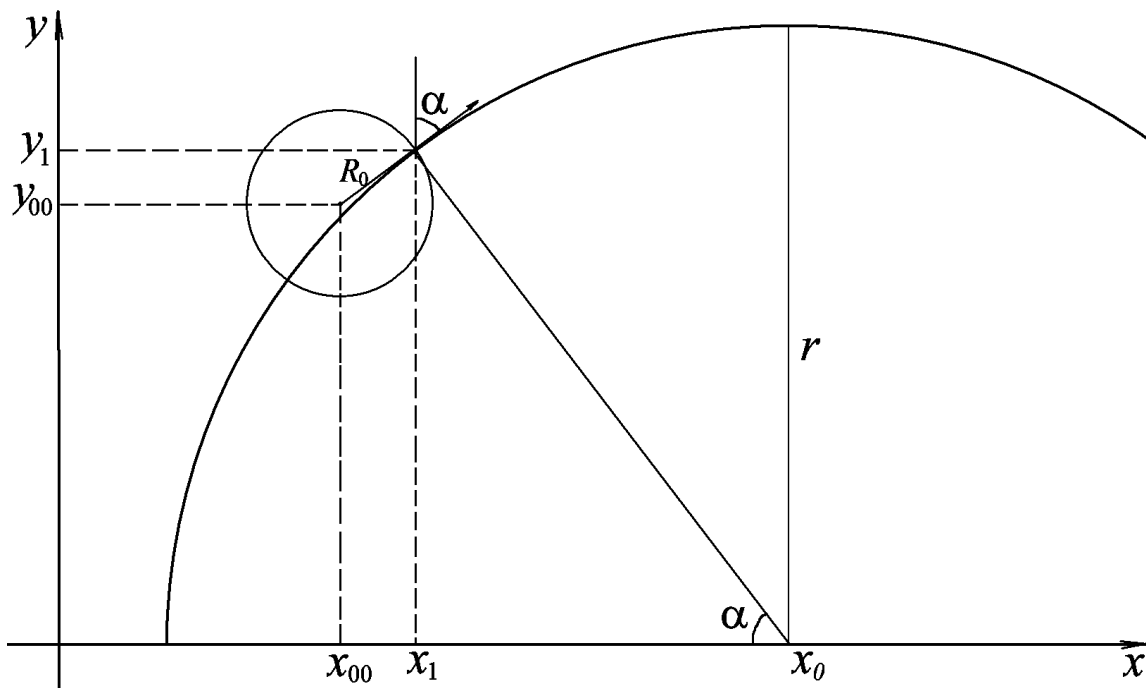


Figure 3.1. The wave-ray trace above the parabolic bottom which exits the circled source boundary point within the angle α relating to the ordinate axis

If, for example, a tsunami source is presented by a circle of radius R_0 with its center located at the point (x_{00}, y_{00}) , then N wave rays start from the source boundary points in the radius-vector directions. Then we will obtain a set of N wave rays coming from the source boundary up to the edges of the computational domain. The scheme of constructing such a ray is shown in Figure 3.1. We will split the whole domain to $N-1$ ray tubes by constructing wave rays exiting N different points, which are equidistantly located around the source. Here it is necessary to take into account the fact that coordinates of the ray starting points (x_i, y_i) vary according to the formulas

$$\begin{aligned} x_i &= x_{00} + R_0 \cdot \sin(\alpha_i), \\ y_i &= y_{00} + R_0 \cdot \cos(\alpha_i). \end{aligned} \tag{3.1}$$

Here α_i is the ray exiting angle according to the ordinate axis. It is not allowed to say that rays reach the shoreline, because from (2.14) it follows that the required travel time for this is infinitely long. Figure 3.2 shows the wave-ray set, which was built using 200 ray exiting points along the circled source boundary. Their exiting angles α_i were equal to $i \cdot \pi/200$ ($i=1, \dots, 200$). Thus, we have obtained the coordinates of the destination point versus the time T and the angle α . Now, with formulas (2.15) - (2.17) we can find the wave front location by fixing the travel time T .

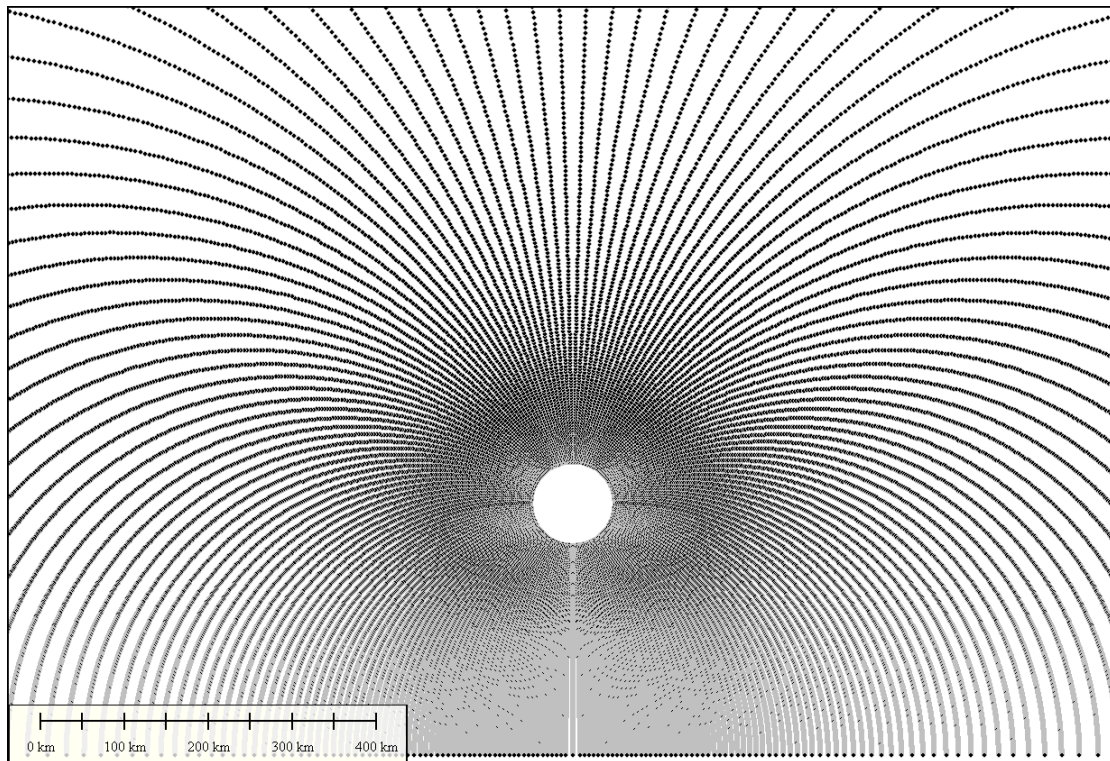


Figure 3.2. Wave-ray traces above the parabolic bottom topography coming from 200 points locating at the circled source boundary

If we draw the lines connecting the points along wave rays corresponding to the same time instance, we will obtain tsunami isochrones. As an example, Figure 3.3 shows positions of the wave front within 5-minutes interval. In this case, the center of the circled source of radius $R_0=50$ km was situated 300 km off the straight shoreline. Here the coefficient k of the parabolic depth growth (2.13) is equal to 10^{-4} . This means that at a distance of 1,000 km off the shore the depth is equal to 10,000 m.

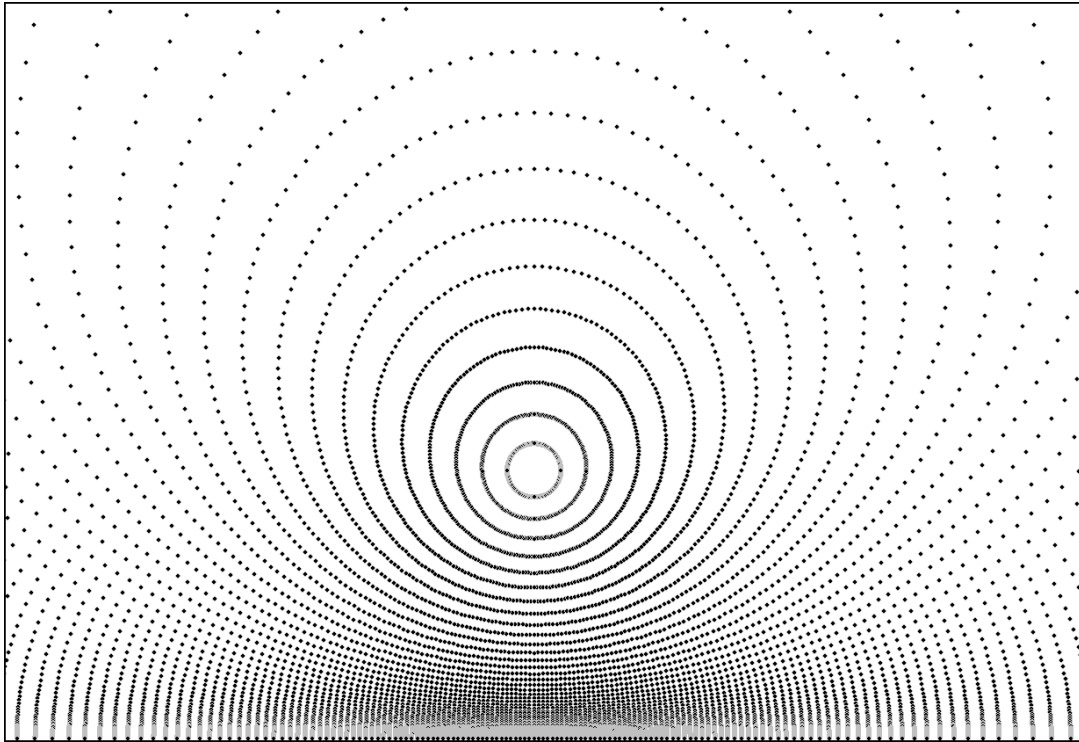


Figure 3.3. Positions of the tsunami wave front (isochrones) within the 5-minutes interval from a circled source of radius 50 km above the parabolic bottom topography

It is possible to prove that over the parabolic bottom topography, the initially rounded wave front will conserve its circle shape at any time instance after the beginning of propagation (Borovskikh, 2006). However, the circle center position will migrate off the shoreline (the lower boundary in Fig. 3.3). If the initial wave front is presented by the circle of radius R_0 with the center located at the distance y_{00} offshore then at a time instance T the circle-shaped wave front radius R_2 and position of its center y_2 can be expressed by formulas

$$R_2 = \left((y_{00} + R_0) \cdot e^{kT\sqrt{g}} - \frac{(y_{00} - R_0)}{e^{kT\sqrt{g}}} \right) / 2, \quad (3.2)$$

$$y_2 = \left((y_{00} + R_0) \cdot e^{kT\sqrt{g}} + \frac{(y_{00} - R_0)}{e^{kT\sqrt{g}}} \right) / 2. \quad (3.3)$$

Here the bottom inclination coefficient k is defined by (2.13). This is one more benchmark solution which can be used for testing numerical methods.

If we want to estimate the wave height at the point (x_1, y_1) it is necessary to determine the distance between the two following points: the first one is the point (x_1, y_1) , where the wave going along the

ray exiting the point $(x_{00}+R_0 \sin \alpha, y_{00}+R_0 \cos \alpha)$ at the angle α (fig. 3.1) arrives at the time T . The second one is the point (x_2, y_2) , where a tsunami wave arrives at the same time moment going along the wave ray exiting the point $(x_{00}+R_0 \sin(\alpha+\Delta\alpha), y_{00}+R_0 \cos(\alpha+\Delta\alpha))$ at the angle $\alpha + \Delta\alpha$. With formula (1.9), the coefficient of wave attenuation due to changing the ray tube width and depth is calculated. Doing this for various values of the time T and the directions of wave rays, we obtain the wave attenuation distribution over the entire area of points which can be reached by the wave rays from the initial wave front points.

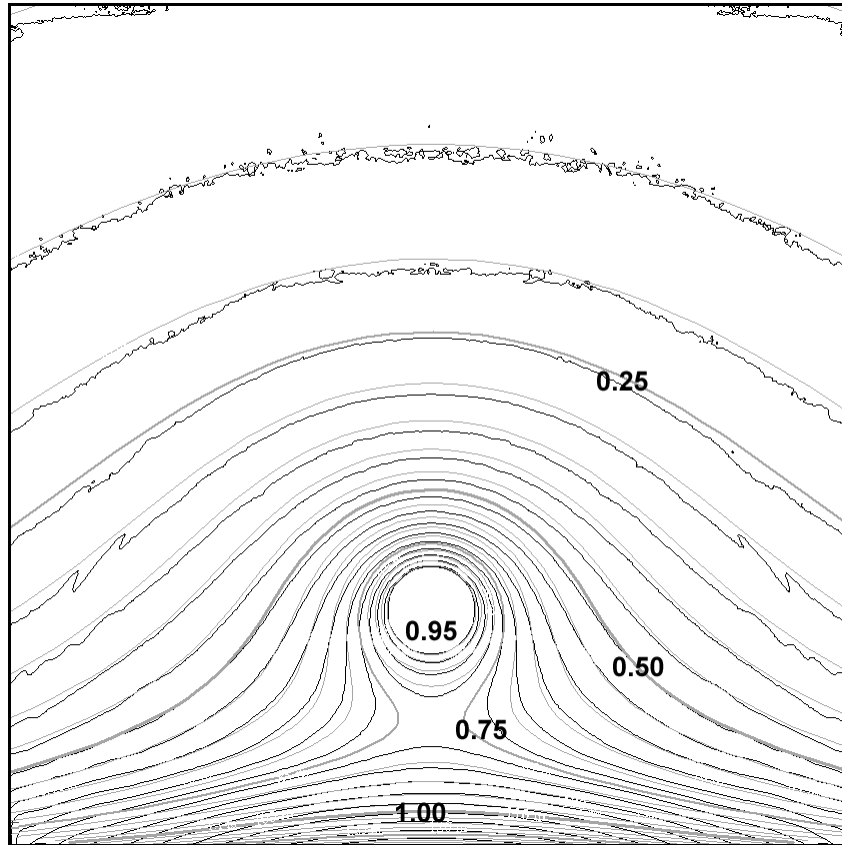


Figure 3.4. The comparative location of the wave-height maxima isolines obtained by numerical calculation of the shallow-water equations (black color) and within the wave-ray approximation (grey color)

To verify the solution obtained, the numerical simulation of the tsunami wave propagation was carried out using the differential shallow-water model with a package called MOST (Titov, 1997). In this numerical experiment the center of a circular source, 40 km in radius, was located at a distance of 300 km from the coast. This source formed a 100-cm high circular wave at a distance of 50 km from the center. This initial front was taken as initial conditions to calculate the amplitudes with the ray model. In Figure 3.4, isolines of the tsunami wave height maxima in the 1000×1000 km coastal area with a parabolic bottom obtained from formulas (2.15)–(2.16) and (1.9) are shown by grey color. For comparison, isolines of the wave height maxima obtained by numerical solution of the same problem

with the nonlinear shallow water model (Titov, 1997) having the same initial values are shown by black color. In both cases, the levels of isolines (whose height is shown in meters), were taken with a spacing of 5 cm. Figure 3.4 shows that the distributions of amplitudes obtained by the two different methods mostly coincide except the shelf area, where a depth is less than 150-200 m where, in contrast to the ray approximation, in the numerical implementation of the differential shallow water model the influence of the nonlinearity is much stronger than in a deep sea.

The parabolic bottom topography (or similar) can be found in several tsunamigenic regions. As an example, the cross-section of the land-bottom relief (Mikheeva et al., 2014) of the Fukushima-Tohoku area (Japan) is presented in Figure 3.5. The white line in this figure shows the cross-section direction.

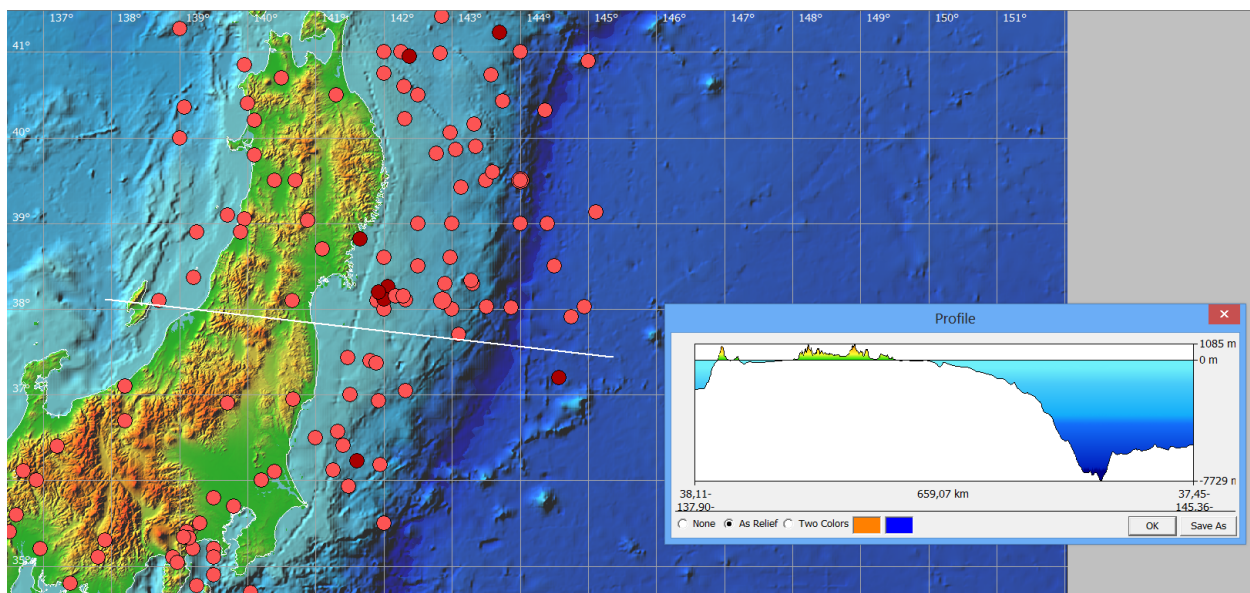


Figure. 3.5. The cross-section of the land-bottom relief through the north of Honshu Island (Japan).

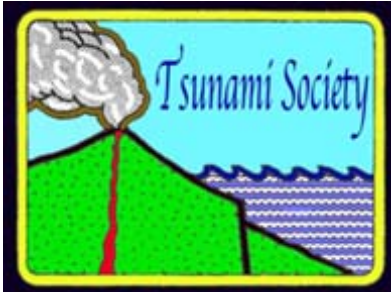
Moreover, one can see that northwards of this cross-section such a kind of bottom topography (parabolic-type) takes place up to the top of Honshu Island.

CONCLUSION

The height of a propagating tsunami wave versus depth and refraction above an uneven bottom has been estimated using the differential shallow-water equations. The exact wave ray trajectory and the tsunami isochrones above the parabolic bottom have been found. A comparison of the results obtained by the ray method and with the shallow water model has been made. This comparison shows that with a numerical method based on the ray approximation not only the arrival times of tsunami waves at different points, but also the wave heights in a deep water can be estimated. These solutions for travel times and wave-ray traces can be used for testing the numerical methods carrying out the tsunami simulation.

REFERENCES

1. Stocker, J.J. (1957). *Water Waves. The Mathematical Theory with Applications.*— New York: Interscience Publishers.
2. Marchuk, An.G., Chubarov, L.B., and Shokin, Yu.I. (1983). *Chislennoe modelirovanie voln tsunami (Numerical Simulation of Tsunami Waves)*, Novosibirsk: Nauka. (In Russian).
3. Marchuk, An.G. (2016). Benchmark solutions for tsunami wave fronts and rays. Part 1: sloping bottom topography. *Science of Tsunami Hazards*, Vol. 35, N 2, 34-48.
4. Romanov, V.G. (1984). *Inverse Problems of Mathematical Physics*, VSP, Netherlands.
5. Sabra, A. I. (1981). *Theories of Light from Descartes to Newton*, Cambridge University Press, (cf. Pavlos Mihas, *Use of History in Developing ideas of refraction, lenses and rainbow*, p. 5, Demokritus University, Thrace, Greece.).
6. Borovskikh, A.V. (2006). The two-dimensional eikonal equation // *Siberian Mathematical Journal*, Volume 47, Issue 5, pp 813–834.
7. Titov, V.V., Gonzalez, F. (1997). Implementation and testing of the method of splitting tsunami (MOST) // Technical Memorandum ERL PMEL-112, National Oceanic and Atmospheric Administration. —Washington DC.
8. Mikheeva, A.V., Vazhenin, A.P., Dyadkov, P.G., Marchuk, An.G. (2014). A study of the spatial-temporal distribution of seismicity around the Fukushima prefecture using the tools of the GIS-EEDB system // *Russian Geoinformatics*, 2, 2-13.



**INVESTIGATION OF b -VALUE VARIATIONS IN THE AFRICAN AND PARTS OF
EURASIAN PLATES**

¹Awoyemi, M. O., ²Hammed O.S., ¹Shode, O. H., ⁴Olurin, O.T., ²Igboama, W.N. and ³Fatoba, J.O.

1. Department of Physics, Obafemi Awolowo University, Ile-Ife, Nigeria.
2. Department of Physics, Federal University, Oye Ekiti, Nigeria.
3. Department of Geophysics, Federal University, Oye Ekiti, Nigeria.
4. Department of Physics, Federal University of Agriculture, Abeokuta, Nigeria.

ABSTRACT

Numerous earthquakes have occurred along the collision zones of the African and parts of Eurasian plates. Some of these earthquakes along these zones have generated tsunamis. To mitigate this hazard, knowledge of b -values of the Gutenberg – Richter relation for tectonic earthquakes in the African and parts of Eurasian plates is essential. The temporal variations of b -values were evaluated using sliding time windows with each window containing a total of 100 events with a view to utilizing the results as a precursor for the earthquake occurrence. The spatial variation of b -values of the study area was also delineated by dividing it into grids and calculating the b -values for each grid using constant radius and constant number of events. Results obtained from the temporal variation of b -values showed that earthquakes of large magnitudes occurred when the b -values were low while earthquakes of small magnitudes occurred when the b -values were high throughout the study period. The results of the spatial distribution of b -values also showed that earthquakes of large magnitudes occurred in areas of low b -values while earthquakes of small magnitudes occurred in areas of high b -values. The study therefore concluded that the temporal and spatial variations of b -values might be considered as a precursor for earthquake prediction.

Keywords: b -value, tsunami, Precursor, Plates, Earthquake, Tectonics.

1.0 INTRODUCTION

The occurrence of destructive earthquakes along the collision zone of African and Eurasian plate boundaries had generated tsunamis in past decades. Despite that there are many uncertainties about the relative motions between the tectonic plates of Africa and Eurasia, continuous continental collision, subduction and crustal shortening processes are still occurring in the zone (Pararas-Carayannis, 2011). From the seismo-tectonic history and estimated rates of these tectonic plate collisions, it is very likely that another destructive earthquake and tsunami similar to the 365 AD and 1303 AD events is statistically long overdue and very likely to occur again in the zone. Such great tsunamigenic earthquakes can be expected to occur every 800 years or so along African and Eurasian plate boundaries (Pararas-Carayannis, 2011).

The African plate is one of the major tectonic plates of the earth where few large earthquakes have been reported. At present, the African plate is the fourth largest tectonic plate (~61 H of Eurasia) a landmass consisting of the traditional continents of Europe and Asia). It also includes oceanic crust extending westward to the Mid - Atlantic Ridge and northward to the Gakkel Ridge.

The African Plate had moved relatively slowly for the last 100 Ma or so in a general northeast direction with a speed estimated at around 2.15 cm (0.85 in) per year, drawing it closer to the Eurasian Plate. However, throughout this period, its continental interior has experienced many seismic changes such as long - term intra - continental crustal deformation which may be due to local and regional tectonic events occurring on the plate (Cloetingh and Burov, 2011; Zoback *et al.*, 1993) and mantle - lithosphere interaction (Heine *et al.*, 2008). Lack of effective seismic monitoring of the plate hampered the study of these events and seismic changes associated with it. To assess these seismic changes for the prediction of future occurrence of earthquakes in the African and parts of Eurasian plates, the knowledge of significant changes in *b*-value is essential. The *b*-value indicates the tectonic character of a region and has been assumed to depend on the accumulated stress in that region. Hence, this study intends to investigate the *b*-value variations in the African and parts of Eurasian Plates.

1.1 Tectonic Settings and Historical Seismicity

The African Plate's speed is estimated at around 2.15 cm (0.85 in) per year. It has been moving over the past 100 million years or so in a general northeast direction, drawing it closer to the Eurasian Plate. The African Plate (Fig.1) is rifting in the eastern interior of the African continent along the East African Rift. This rift zone represents a zone of maximum weakness where the African Plate is deforming, as plates to its east are moving rapidly northward.

The highest seismicity of the African continent is concentrated in East Africa. Recent seismicity demonstrates that the East African rift is prone to large earthquakes, since some of the strongest events of the 20th century exceeded $M = 7$, such as that of the 13 December, 1910; Rukwa, Tanzania ($MS = 7.4$), 20 and 24 May 1990, Sudan ($MS = 7.0 - 7.4$), and 22 February 2006, Mozambique ($MW = 7.0$) (Mourabit *et al.*, 2013).

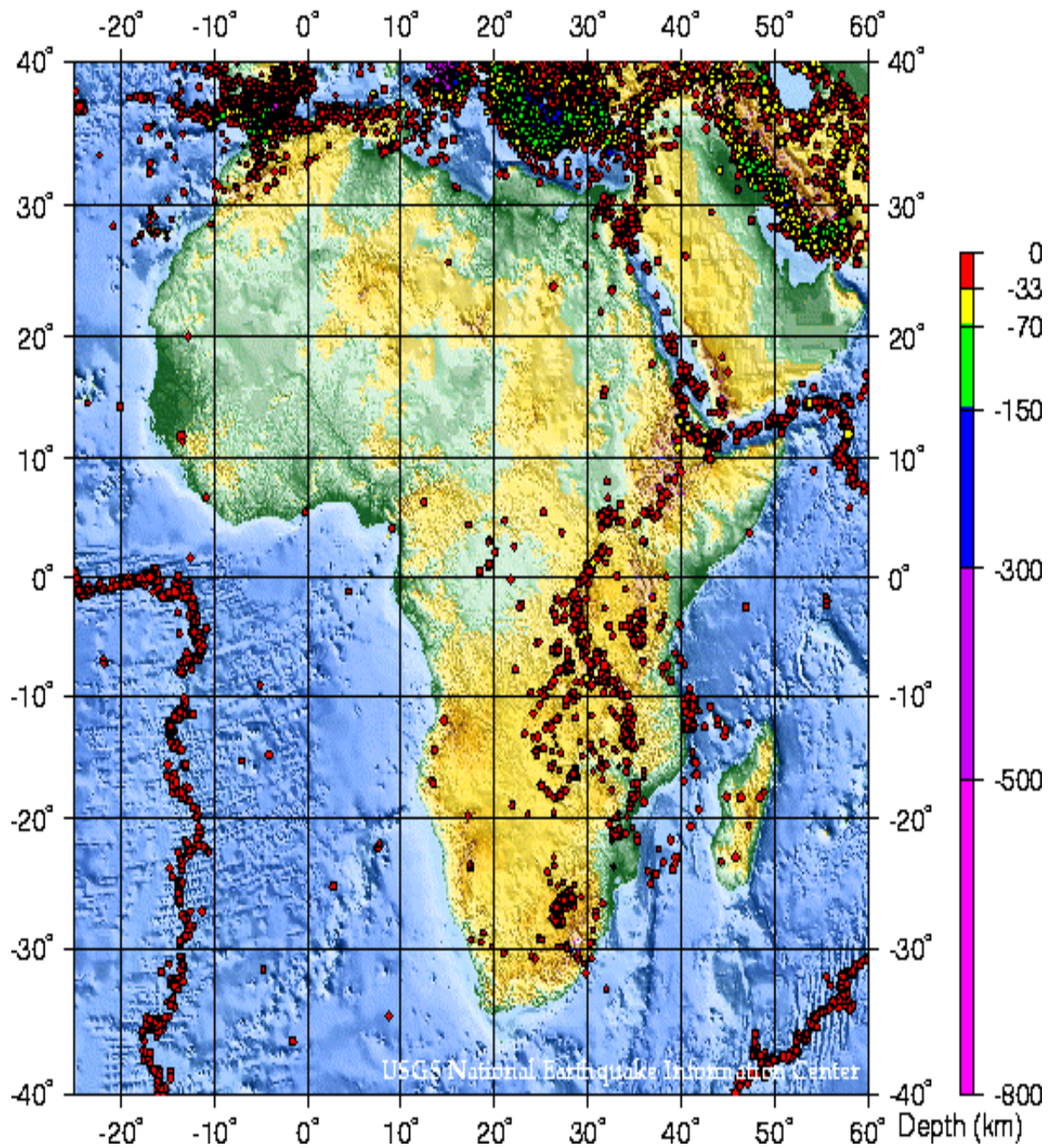


Figure 1: Seismicity Map of the Study Area [Source: National Earthquake Information Center (NEIC), US Geological Service.]

In North Africa, Algeria is known as one of the most active region because several large and shallow depth (0 – 30 km) earthquakes have occurred in the last six decades [Orléanville, (1954, $MS=6.0$), El Asnam, (1980, $M 7.3$), Constantine (1985, $MS 6.0$), Tipasa - Chénoua (1989, $MS 6.0$), Mascara, (1994, $M 6.0$) and Zemmouri, (2003, $M 6.8$)].

Large earthquakes have also been reported in countries such as Morocco, Libya, and Egypt. In February 2004, the city of Al Hoceima and the Rif Mountains of Morocco were struck by a large earthquake ($MW=6.4$), 10 years after the May 1994 ($MS=6.0$) event. The city of Cairo in Egypt was struck in October 1992 by an earthquake of magnitude 5.8, which caused large damage. In 1935, the Syrte region in Libya experienced an earthquake of magnitude 6.9 with severe damage (Suleiman and Doser 1995; Suleiman *et al.*, 2004).

Seismic activities in Southern Africa are believed to be an extension of the East Africa rift system. South Africa has experienced few major earthquake events. Among these is the earthquake of Orange Free State in 1912. Historically, the most severe earthquake of magnitude 6.3 on the Richter scale occurred on 29 September 1969 in Ceres, 100 km northeast of Cape Town (Alabi *et al.*, 2013).

Central and Western Africa, is generally considered as aseismic or having low seismicity. The biggest magnitude recorded is $MW = 6.5$ in Ghana and $MW = 6.0$ in Cameroon. Though Nigeria is not located within the major earthquake zones of the world, nevertheless it has experienced series of earth tremors especially in the southwestern part. The first reported occurrence of an earth tremor in Nigeria was in 1939 in Lagos, Ibadan and Ile - Ife located in the south - western part of the country. Subsequent occurrences of earth tremors in Nigeria were in 1984, 1988, 1990, 1997, 2000 and 2006. The intensities of these shocks ranged from III to IV on the Modified Mercalli Intensity Scale (Akpan and Yakubu ,2010).

Several seismic events have also occurred in Accra, Ghana, extending along the Akwapin faults to the Volta River (Burke, 1969). In the past 120 years, Accra has on three occasions been damaged by major earthquakes in 1906, 1939, and 1941 (Junner, 1941).

On December 22, 1983, a large earthquake also occurred in Guinea further west of Nigeria in an area, which was previously considered aseismic (USGS location 11.93 S and 13.60 W) (Dorbarth *et al.*, 1983). Seiberg (1932) also reported five earthquakes from Cameroon of which two were associated with the Cameroon mountain volcano and two including the largest had epicenters at Kribi (100 E, 40 N), 200 km to the south.

1.2 The *b*-value

In the year 1956, Charles Francis Richter and Beno Gutenberg proposed the relationship between earthquake magnitude and frequency in what they called the Gutenberg-Richter relation. This Gutenberg-Richter relation which is also known as the Frequency-Magnitude Distribution (FMD) is commonly used in the modeling of earthquake hazard, mostly related to the earthquake precursors and

probabilistic seismic hazard assessments (Nuannin, 2006; Damanik *et al.*, 2010). The FMD describes the number of earthquakes occurring in a given region as a function of their magnitude M as:

$$\log N = a - bM \quad (1)$$

where N is the cumulative number of earthquakes with magnitudes equal to or greater than M , and a and b are real constants whose values varies in time and space. The parameter a characterizes the general level of seismicity in a given area during the study period, that is the higher the a value, the higher the seismicity. The parameter b commonly called the b -value has been widely used in the studies of seismicity, tectonics, seismic risk estimation and earthquakes prediction. The b -value indicates the tectonic character of a region and assumed to depend on the accumulated stress in that region (Nuannin, 2006). Schorlemmer *et al.* (2004) described b -value as a stress meter, depending inversely on the differential stress.

Regionally, changes in b -value are believed to be inversely related to changes in the stress level (Bufe, 1970; Gibowicz, 1973). An increase of applied shear stress or effective stress results in decrease of b -value (Urbancic *et al.*, 1992; Wyss, 1973). A smaller b -value probably means that the stress is high in the examined region. Decreasing b -value within the seismogenic volume under consideration has been found to correlate with increasing effective stress levels prior to major shocks (Kanamori, 1981). Studies revealed that the b -value is also related to the depth of occurrence of the earthquake (Weimer and Benoit, 1996; Mori and Abercrombie, 1997; Wyss *et al.*, 1997, 2001).

In general, the b -value in broad seismic regions is close to 1.0 from global statistics (Lay and Wallace, 1995). For regions in smaller scale over a few to tens of kilometers, the temporal and spatial variations in b -values may be significantly large, ranging from 0.5 to 1.5 in Japan (Ogata and Katsura, 1993) and from 0.5 to 1.3 near Parkfield of the San Andreas fault (Schorlemmer *et al.*, 2004). Variation of b -value in a region is commonly correlated with characteristics of regional seismic activities. For example, high seismicity in magma chambers may be characterized by high b -values (Sanchez *et al.*, 2004; Wiemer and McNutt, 1997). The initial rupture of large earthquakes, by contrast, was found to occur in regions where b -values were low (Wyss and Stefansson, 2006; Wyss *et al.*, 2000). Schorlemmer *et al.* (2005) pointed out that the region with low b -value implies large differential stress and suggests its being toward the end of the seismic cycle. Such relationship can be applied for evaluating seismic hazard and earthquake forecasting (Smith, 1981).

The b -value in Equation (1) can be estimated either by linear least squares regression or by maximum - likelihood method (Aki, 1965; Ustu, 1965; Bender, 1983; Nuannin, 2006; Damanik *et al.*, 2010). In this study, the maximum - likelihood method has been used to calculate b -value. The maximum - likelihood estimate of the b -value is given as (Öztürk, 2012):

$$b = 2.303M - M \min + 0.005 \quad (2)$$

where M indicates the average magnitude and $M \min$ is the minimum magnitude of the local catalog data that is being investigated. Value 0.005 in Equation 2 is a correction constant.

2.0 DATA ACQUISITION, DESCRIPTION AND METHOD.

Earthquake data used for this study were extracted from the Advanced National Seismic System (ANSS) Comprehensive Catalog, a website of Northern California Earthquake Data Centre (NCEDC), USA (<http://quake.geo.berkeley.edu/anss/catalog-search.html>). The data covered a region bounded by latitudes -40° to $+40^{\circ}$ and longitudes -20° to $+60^{\circ}$ which comprises of the African and parts of Eurasian plates. The data were obtained in a readable format for earthquakes with magnitude and depth ranging from $MW = 2.0$ to $MW = 7.7$ and 0 to 700 km respectively, for a period of forty years (1/8/1975 to 31/7/2015). There were 73,389 earthquakes in all. Each datum composed the date of occurrence of earthquake, origin time, coordinates of epicenter, magnitude, event identification, and focal depth of earthquake.

2.1 Frequency – Magnitude Distribution (FMD) of Earthquakes

The Frequency – Magnitude Distribution (FMD) of earthquakes that took place in the study area for the forty-year periods of study was evaluated. This was done by plotting the cumulative number of earthquakes as a function of their magnitudes. These plots were then fitted with a straight line that best fit the plots. The straight line represents the Gutenberg – Richter equation. The magnitude of completeness M_C of the earthquake catalogue also known as the threshold magnitude which is the magnitude above which all earthquakes were recorded was then determined from the plots. The overall b -value of earthquakes from the study area was determined by finding the slope of the line of best fit while the a -value, that is, the seismicity level of the study area was also determined by substituting the known parameters into the Gutenberg – Richter equation. Figure 2 showed the Frequency – Magnitude Distribution of earthquakes in the study area for the forty-year periods of study. From Figure 2, we have $M_C = 4.7$, $b = 1.18$, and $a = 10.4$.

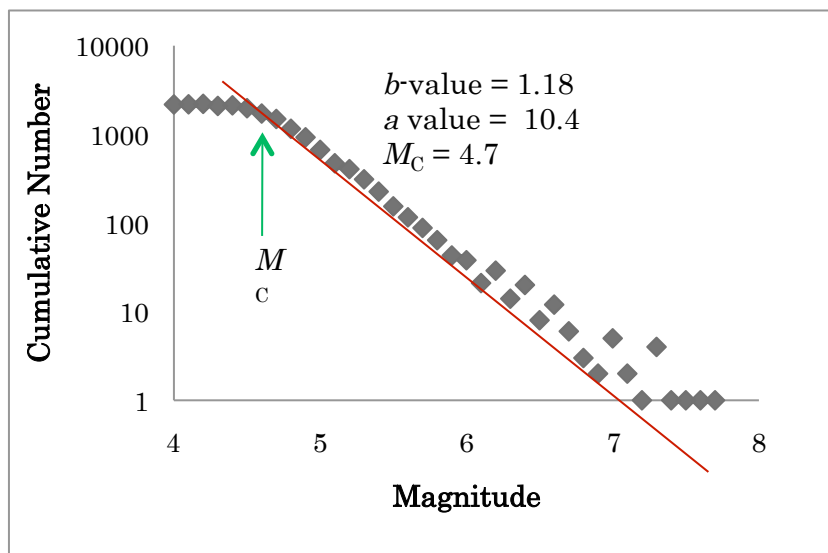


Figure 2: Frequency – Magnitude Distribution (FMD) of Earthquakes from August 1, 1975 to July 31, 2015. The Red Thin
Vol 36. No. 2, page 91 (2017)

2.2 Temporal Variation of b -value

To study variations of b -value with time, a sliding time window method was used. Due to high difference between the numbers of events in each window, constant number of events in each window was considered. A group of earthquakes was chosen from the earthquake catalogue and the b -value was calculated for the first window using the maximum likelihood equation. The window was then shifted by a time corresponding to certain number of events. The b -value was calculated for the new group of data and the process was repeated until the last window was reached. For this study, 100 events in windows have been selected which was shifted for every year. Several tests were performed by varying the number of events in the window i.e. 50, 100, 150 and 200. Varying the step (shift) length was also tested but it does not affect the resolution.

Figures 3, 4, 5 and 6 showed the temporal variations of b -values for ten years each of the periods of study while Figure 7 showed the temporal variation of b -values for the forty – year periods of study.

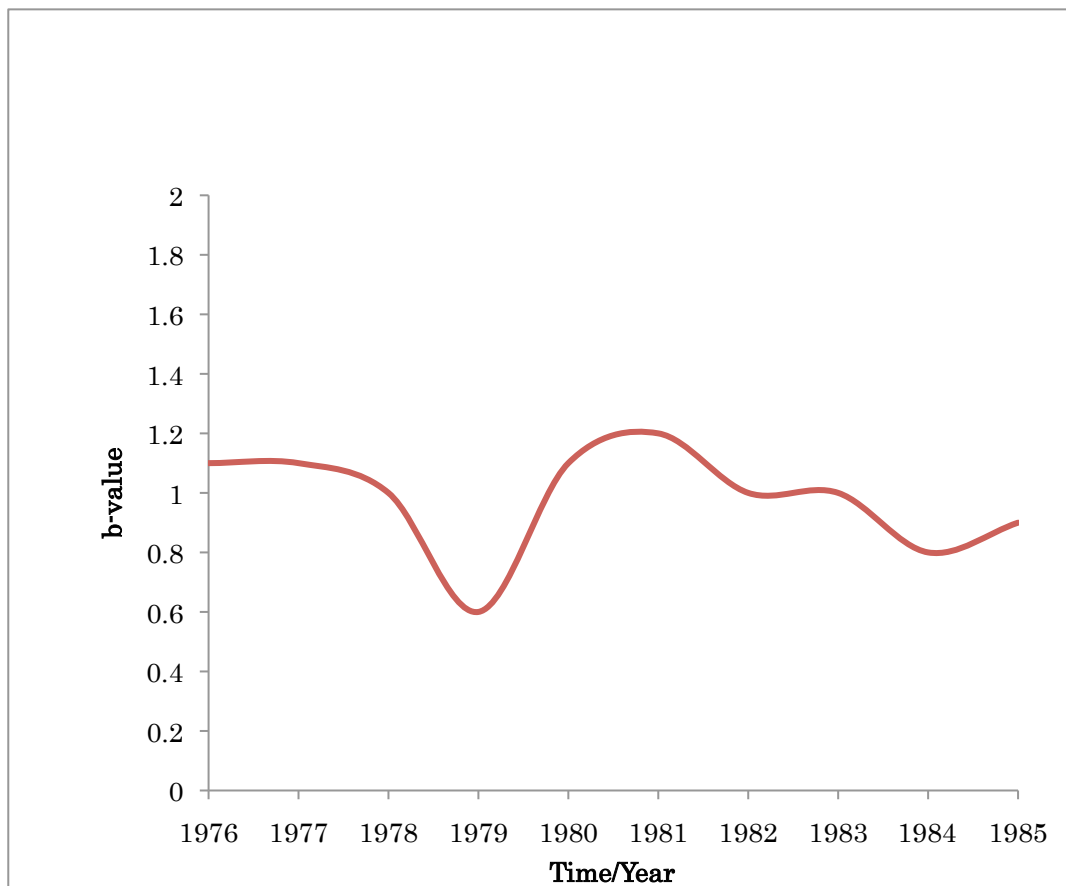


Figure 3: Temporal Variation of b -value from August 1, 1975 to July 31, 1985.

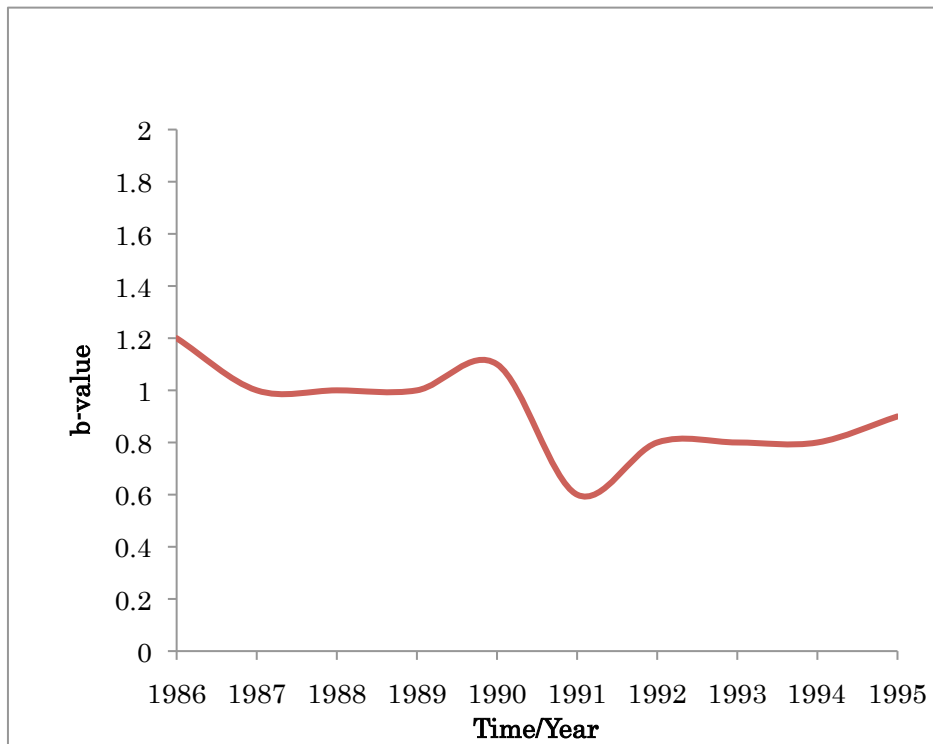


Figure 4: Temporal Variation of b -value from August 1, 1985 to July 31, 1995.

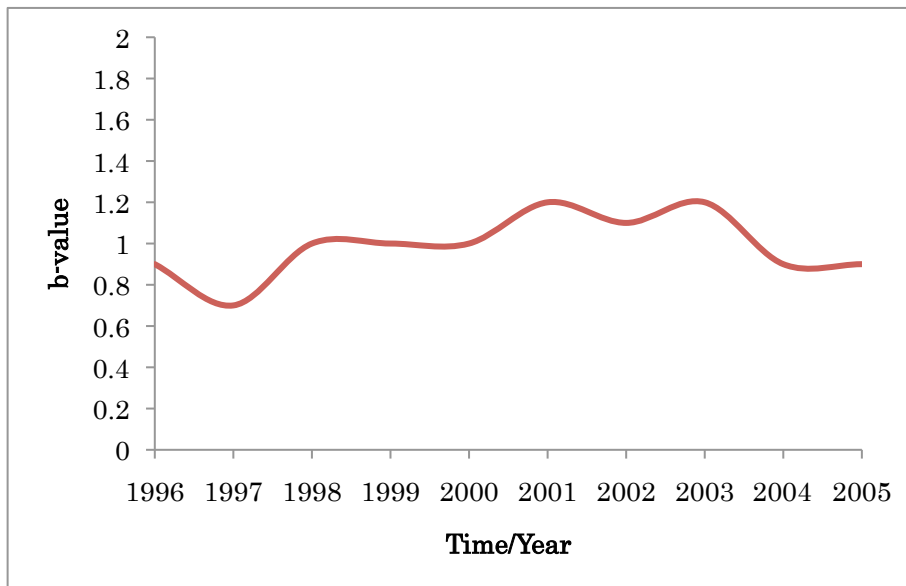


Figure 5: Temporal Variation of b -value from August 1, 1995 to July 31, 2005.

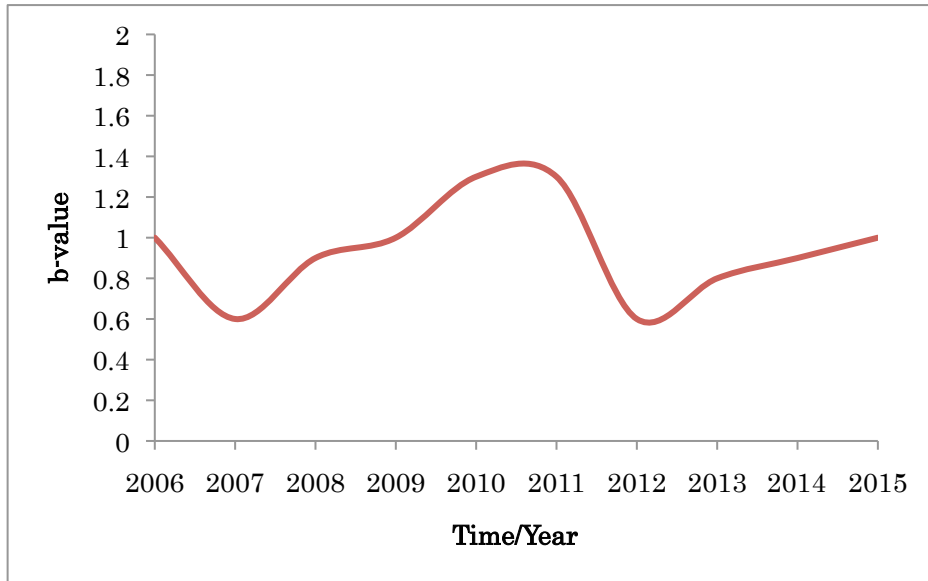


Figure 6: Temporal Variation of b -value from August 1, 2005 to July 31, 2015.

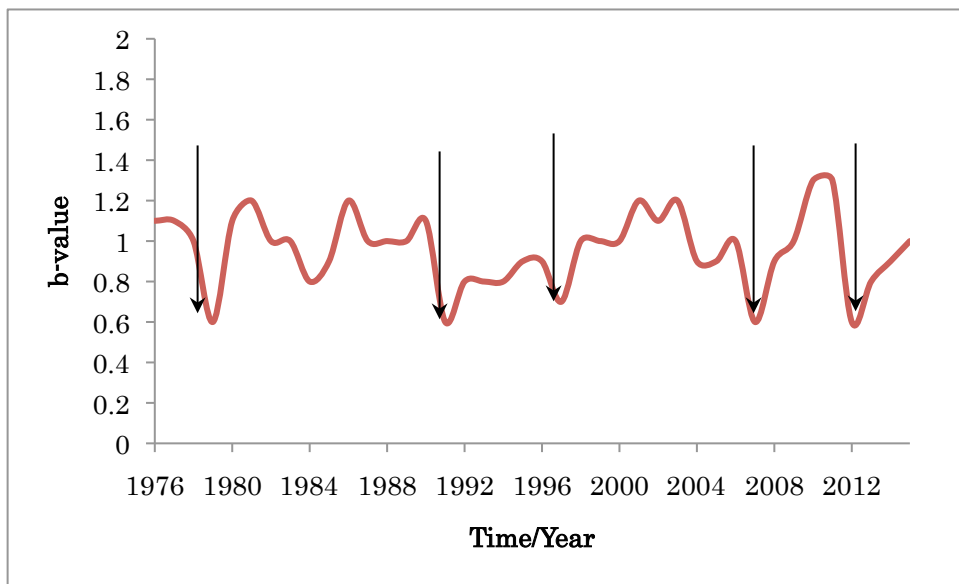


Figure 7: Temporal Variation of b -value from August 1, 1975 to July 31, 2015 as Thick Red Line. Arrows Mark the Occurrence Time of Large Earthquakes ($M \geq 5.4$)

2.3 Spatial Variation of b -value

The spatial variation of b -values was mapped by projecting earthquake epicenters onto a plane. The study area was divided into grids and b -values were calculated for each grid using constant radius and constant number of events. In this study, the spatial variation of b -value was determined using a $10^\circ \times 10^\circ$ processing grid with each grid containing a total of 100 events. To visualize the variation of b -value with space, the b -values were gridded using minimum curvature gridding method and were displayed using a color-shaded map. Figure 8 showed the spatial variation of b -values for the study area.

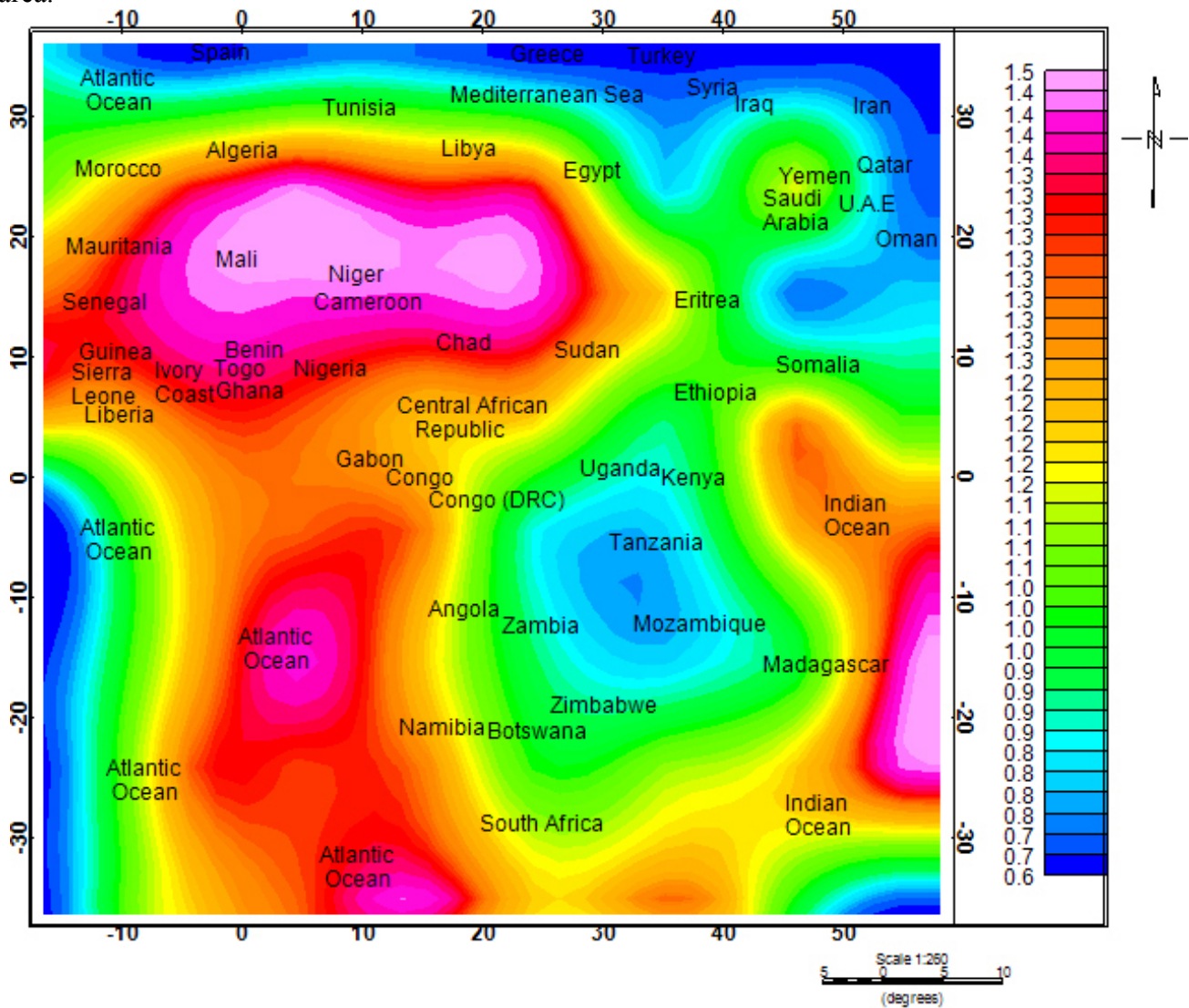


Figure 8: Spatial Variation of b -values for the Forty – Year Period of Study.

3.0 RESULTS AND DISCUSSION

The overall b -value of earthquakes from the study area for the entire periods of study was estimated to be 1.18 as shown in Figure 2. From the temporal variations of b -values (Figures 3, 4, 5, 6, and 7), it was observed that the b -value varies between 0.6 and 1.3 throughout the study period. High b -values were observed in the years 1976, 1977, 1980, 1981, 1986, 1990, 2001, 2002, 2003, 2010 and 2011. In these years the b -values ranges from 1.1 to 1.3. These years have the lowest average magnitude of earthquakes (between 4.1 and 4.4) as they were dominated by numerous earthquakes of small magnitudes.

The years 1978, 1982, 1983, 1984, 1985, 1987, 1988, 1989, 1992, 1993, 1994, 1995, 1996, 1998, 1999, 2000, 2004, 2005, 2006, 2008, 2009, 2013, 2014 and 2015 experienced a slight decrease in b -value. For these years, b -values vary between 0.8 and 1.0. The average magnitude of earthquakes that took place during these periods was between 4.5 and 4.9. These years were dominated by few earthquakes of large magnitudes.

The lowest b -values observed were between 0.6 and 0.7 and were recorded in the years 1979, 1991, 1997, 2007 and 2012. These years experienced the highest average magnitude of earthquakes (between 5.0 and 5.5) as they were dominated by numerous earthquakes of large magnitudes.

From the spatial variation of b -values (Fig. 8), we found the clustering of low b -value along the African – Eurasian plate boundary, in countries such as Spain, Greece and Turkey as well as parts of Atlantic and Indian Oceans. All these areas were shown in blue color and they have variations of b -values ranging from 0.6 to 0.7. Low b -values were also observed in some East African countries such as Uganda, Kenya, Tanzania, Zambia, Mozambique and Zimbabwe as well as some Arabian countries such as Syria, Iraq, Iran, Qatar, United Arab Emirates and Omar. These areas were shown in light blue color and they have variations of b -values ranging from 0.8 to 0.9. These areas have high level of seismicity and have experienced numerous earthquakes of large magnitudes. The average magnitude of earthquakes that took place in these region ranges from 4.6 to 5.5.

The areas marked by green color in the b -value distribution map are those areas that experienced just few earthquakes of intermediate magnitudes. The b -value for these regions ranges from 1.0 to 1.1. The average magnitude of earthquakes that took place in these regions was between 4.3 and 4.6. These areas include Tunisia, Egypt, Yemen, Saudi Arabia, Eritrea, Somalia, Ethiopia, Congo (DRC), Angola, Botswana, Madagascar and South Africa as well as parts of Indian and Atlantic Oceans. Areas shown in yellow are areas of high b -values. These areas have low seismicity as they were dominated with numerous earthquakes of small magnitudes. The b -value for these areas ranges from 1.2 to 1.3 and the average magnitudes of earthquakes that took place in these regions was between 4.1 and 4.3. These areas include Morocco, Algeria, Libya, Namibia, Congo, Gabon, Central African Republic, Sudan, Chad, Nigeria, Ghana, Ivory Coast, Sierra Leone, Liberia, Guinea, Senegal and Mauritania.

The areas shown in pink represent areas of very low or no seismicity. These represent areas where the total number of earthquake that occurred was not up to the total number of earthquakes used for the calculation of b -value in this study or areas where no significant earthquake was recorded during the period of the study. The b -values for these regions range from 1.4 to 1.5. These areas include Benin, Togo, Cameroon, Mali and Niger and some parts of Indian and Atlantic Oceans.

4.0 CONCLUSION

The variation of b -value with time and space has been successfully investigated for earthquakes in the African and parts of Eurasian plates. Results obtained from the temporal variations of b -values showed that earthquakes of large magnitudes occurred when b -values were low throughout the study period while earthquakes of small magnitudes occurred when b -values were high. Significant drops in b -values revealed a U-shape curve in the b -value versus time graphs. A rapid increase of b -value with time was also observed after the occurrence of large earthquakes. Also, from the results obtained from the geographical distribution of b -values, it was observed that earthquakes of large magnitudes occurred in regions of low b -values while earthquakes of small magnitudes occurred in regions of high b -values. This study therefore concluded that the temporal and spatial variations of b -values might be considered as a precursor for earthquake prediction. Hence, this study suggests that monitoring the b -value variations in the African and parts of Eurasian plates may be a useful method for predicting likely occurrence of earthquakes in the study area.

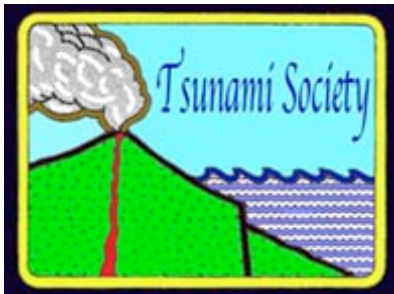
REFERENCES

- Aki, K. 1965. Maximum - Likelihood Estimate of b in the Formula $\log N = a - bM$ and Its Confidence Limits. *Bulletin of the Earthquake Research Institute* 43: 237 - 239
- Alabi, A. A., Olukayode, D. A. and Adebambo A. 2013. Seismicity Pattern in Southern Africa from 1986 to 2009. *Earth Science Research* 2: 2
- Akpan, O.U. and Yakubu, T.A. (2010) A Review of Earthquake Occurrences and Observations in Nigeria. *Earthquake Science*, **23**, 289-294.
- Bufe, C. G. 1970. Frequency - Magnitude Variations during the 1970 Danville Earthquake Swarm. *Earthquake Notes* 41: 3 - 6
- Burke, K. 1969. Seismic Areas of the Guinea Coast where Atlantic Fracture Zones Reach Africa. *Nature* 222 (5194): 655 - 657
- Cloetingh, S. and Burov, E. 2011. Lithospheric Folding and Sedimentary Basin Evolution: A Review and Analysis of Formation Mechanisms. *Basin Research* 23: 257 – 290
- Damanik, R., Andriansyah, Putra, H. K., Zen, M. T. 2010. Variations of b -values in the Indian Ocean – Australian Plate Subduction in South Java Sea. *Proceedings of the Bali 2010 International Geosciences Conference and Exposition, Bali, Indonesia*: 19 - 22
- Dorbarth, L., R. Caulon, T. George, and P. Mogue. 1983. Guinean Earthquake of December 22, 1983. *Tectonophysics* 82: 112 – 124

- Gibowicz, S. J. 1973. Variation of the Frequency-Magnitude Relation during Earthquake Sequences in New Zealand. *Bulletin of the Seismological Society of America* 63: 517 – 528
- Pararas-Carayannis, G. 2011. The earthquake and tsunami of July 21, 365 AD in the Eastern Mediterranean Sea - Review of impact on the ancient world - assessment of recurrence and future impact. 30 (4): 286
- Heine, C., Muller, R. D., Steinberger, B. 2008. Subsidence in Intra - continental Basins Due to Dynamic Topography. *Physics of the Earth and Planetary Interiors* 171: 252 – 264
- Junner, N. R. 1941. The Accra Earthquake of 22nd June, 1939. *Gold Coast Geological Survey* 13
- Kanamori, H. 1981. The Nature of Seismic Patterns before Large Earthquakes. In Earthquake Prediction: An International Review. *American Geophysical Union* 4: 1 - 19
- Lay, T. and Wallace, T. C. 1995. Modern Global Seismology. Academic Press: 393
- Mori, J., and R. E. Abercrombie 1997. Depth Dependence of Earthquake Frequency Magnitude Distributions in California: Implication for the Rupture Initiation. *Journal of Geophysical Research* 102: 15, 81 - 90
- Mourabit, T., Abou Elenean, K., Ayadi, A., Benouar, D. and Ben Suleman, A. 2013. Neo - deterministic Seismic Hazard Assessment in North Africa. *Journal of Seismology*
- Nuannin, P. 2006. The Potential of *b*-value Variations as Earthquake Precursors for Small and Large Events. *Digital Comprehensive Summaries of Uppsala Dissertations from the Faculty of Science and Technology*
- Ogata, Y. and Katsura, K. 1993. Analysis of Temporal and Spatial Heterogeneity of Magnitude Frequency Distribution Inferred From Earthquake Catalogues. *Geophysical Journal International* 113: 727 – 738
- Ozturk, S. 2012. Statistical Correlation Between *b*-value and Fractal Dimension Regarding Turkish Epicentre Distribution. *Earth Sciences Research Journal* 16: 103 - 108
- Sanchez, J. J., McNutt, S. R., Power, J. A. and Wyss, M. 2004. Spatial Variations in the Frequency – Magnitude Distribution of Earthquakes at Mount Pinatubo volcano. *Bulletin of the Seismological Society of America* 94: 430 – 438
- Schorlemmer, D., S. Wiemer, and M. Wyss 2004. Earthquake Statistics at Parkfield I: Stationarity of *b*-values. *Journal of Geophysical Research* 109
- Schorlemmer, D., Wiemer, S., and Wyss, M. 2005. Variations in Earthquake Size Distribution across Different Stress Regimes. *Nature* 437 (22): 539 – 542
- Seiberg, A. 1932. Handbuck der Geophysik. Berlin, Germany. *Seismological Society of America* 62: 435 – 687
- Smith, W. D. 1981. The *b*-values as an Earthquake Precursor. *Nature* 289: 136 – 139
- Suleiman A. S. and Doser D. I. 1995. The Seismicity, Seismotectonics and Earthquake Hazards of Libya, With Detailed Analysis of the 1935 April 19, *M* = 7.1 Earthquake Sequence. *Geophysical Journal International* 120: 312 - 322
- Suleiman A. S., Albini P. and Migliavacca P. 2004. A Short Introduction to Historical Earthquakes in Libya. *Annals of Geophysics* 47: 2 - 3, 545 - 554
- Urbancic, T. I., C. I. Trifu, J. M. Long, and R.P. Young 1992. Space - Time Correlation of *b*-values with Stress Release: 449 - 462
- Ustu, T. 1965. A Method in Determining the Value of *b* in a formula $\log N = a - bM$ Showing the Magnitude Frequency For Earthquakes. *Geophysical Bulletin of Hokkaido University* 13: 99 – 103

- Wiemer, S. and J. Benoit 1996. Mapping the *b*-value Anomaly at 100 km depth in the Alaska and New Zealand Subduction Zones. *Geophysical Research Letters* 23: 1557 - 1560
- Wiemer, S. and McNutt, S. 1997. Variations in Frequency – Magnitude Distribution with Depth In Two Volcanic Areas: Mount St. Helens, Washington, and Mt. Spurr, Alaska. *Geophysical Research Letters* 24: 189 – 192
- Wyss, M. 1973. Towards a Physical Understanding of Earthquake Frequency Distribution. *Geophysical Journal International* 31: 341 – 359
- Wyss, M. and Stefansson, R. 2006. Nucleation Points of Recent Mainshocks in Southern Iceland, Mapped by *b*-values. *Bulletin of the Seismological Society of America* 96: 599 – 608
- Wyss, M., F. Klein, K. Nagamine, and S. Wiemer 2001. Anomalously High *b*-values in the South Flank of Kilauea Volcano, Hawaii: Evidence for the Distribution of Magma below Kilauea's East Rift Zone. *Journal of Volcanic and Geothermal Research* 106: 23 - 37
- Wyss, M., K. Shimazaki, and S. Wiemer 1997. Mapping Active Magma Chambers by *b*-value Beneath the Off - Ito Volcano, Japan. *Journal of Geophysical Research* 102: 20413 - 20422
- Wyss, M., Schorlemmer, D. and Wiemer, S. 2000. Mapping Asperities by Minima of Local Recurrence Time: The San Jacinto - Elsinore Fault Zones. *Journal of Geophysical Research* 105: 7829 – 7844
- Zoback, M. D., Stephenson, R. A., Cloetingh, S., Larsen, B. T., Vanhoorn, B., Robinson, A., Horvath, F., Puigdefabregas, C., Benavraham, Z., 1993. Stresses in the Lithosphere and Sedimentary Basin Formation. *Tectonophysics* 226: 1 – 13

ISSN 8755-6839



SCIENCE OF TSUNAMI HAZARDS

Journal of Tsunami Society International

Volume 36

Number 2

2017

Copyright © 2017 - TSUNAMI SOCIETY INTERNATIONAL

TSUNAMI SOCIETY INTERNATIONAL, 1741 Ala Moana Blvd. #70, Honolulu, HI 96815, USA.

WWW.TSUNAMISOCIETY.ORG